Icarus 388 (2022) 115219

Contents lists available at ScienceDirect

Icarus

journal homepage: www.elsevier.com/locate/icarus

Research Paper

A numerical study of the liquid motion in Titan's subsurface ocean

David Vincent [a,*], Jonathan Lambrechts [a], Robert H. Tyler [b,c], Özgür Karatekin [d], Véronique Dehant [d,e], Éric Deleersnijder [f]

[a] Université Catholique de Louvain, Institute of Mechanics, Materials and Civil Engineering (IMMC), Avenue Georges Lemaître 4, B-1348 Louvain-la-Neuve, Belgium
[b] NASA Goddard Space Flight Center, Geodesy and Geophysics Laboratory Code 61A, Greenbelt MD, 20771, USA
[c] Joint Center for Earth Systems Technology, University of Maryland, Baltimore County, USA
[d] Royal Observatory of Belgium, Avenue Circulaire 3, B-1180 Bruxelles, Belgium
[e] Université Catholique de Louvain, Earth and Life Institute (ELI), Croix du Sud 2, B-1348 Louvain-la-Neuve, Belgium
[f] Université Catholique de Louvain, Institute of Mechanics, Materials and Civil Engineering (IMMC) & Earth and Life Institute (ELI), Avenue Georges Lemaître 4, B-1348 Louvain-la-Neuve, Belgium

ARTICLE INFO

Keywords:
Titan
Subsurface ocean
Liquid tides
Oceanography
SLIM

ABSTRACT

An ocean filled with liquid water lies beneath the icy surface of several Jovian and Saturnian moons. In such an ocean, the currents are driven by various phenomena such as the tidal forcing, the deformation of the ice shell lying at its top, the temperature gradient resulting from the surface and bottom heat fluxes…The flow induced by the first two forcings can be modelled by means of a 2D depth-averaged model, while the third one generates horizontal and vertical density variations whose effects can only be captured by a 3D baroclinic model.

We study the tides of Titan's subsurface ocean and the impact of the ice shell on the liquid motion by means of the Second-generation Louvain-la-Neuve Ice–ocean Model, SLIM (https://www.climate.be/slim). The impact of the ice shell lying at the top of the ocean is modelled by a surface friction term and surface pressure terms. The latter are a function of the difference between the ocean elevation and the vertical displacement of the shell and the time derivative of this difference.

Because of Titan's appreciable obliquity (0.306°), the tidal motion expected (and found) is similar to the Europa tidal scenario described by Tyler (2008): the surface elevation consists of two bulges rotating around Titan and the associated depth-averaged velocity field consists of two gyres, separated by an area of high speed flow, whose centre follows a sinusoidal path centred on the equator. The ice shell damps the surface motion, thus slowing down the flow, without significantly modifying the spatial patterns of these fields. The depth of the ocean and the mechanical characteristics of the ice shell being poorly constrained, a sensitivity analysis is conducted. The depth-averaged flow slows down when the depth is increased and a lag appears in the tidal phase but the tidal range remains similar. The ice shell mechanical characteristics influences both the elevation and depth-averaged velocity fields in terms of magnitude but does not modify the spatial patterns of these fields.

The influence of the surface heat flux is studied by means of the 3D baroclinic version of SLIM. The heat flux derived from Titan's topography by Kvorka et al. (2018) is used as surface boundary condition for the temperature equation while a uniform bottom heat flux is implemented. Its value is computed assuming that the heat budget of the ocean is at equilibrium. These boundary conditions cause density variations, which impact the hydrodynamics of the ocean. While the flow velocity induced by these variations is two orders of magnitude smaller than the tidal flow, its orientation is time-independent, hence impacting the orientation of the velocity field. Although the variations of ocean surface elevation and speed with respect to the shell mechanical properties can be larger than those induced by the surface heat flux, taking into account the latter results in large variations of the velocity field global patterns, which was not observed when modifying the shell mechanical properties. Future studies should therefore focus on modelling the surface and bottom heat fluxes while uncertainties about the mechanical characteristics of the shell can be tolerated.

* Corresponding author.
E-mail address: david.vincent@uclouvain.be (D. Vincent).

https://doi.org/10.1016/j.icarus.2022.115219
Received 5 January 2021; Received in revised form 29 April 2022; Accepted 8 August 2022
Available online 17 August 2022

1. Introduction

Several celestial bodies in our Solar System hide liquid layers beneath their surface. Such layers modify the magnetic field, the ability to deform, and the shape of the celestial body. The layers can be filled with molten metal (Mercury and Earth), liquid hydrogen (Jupiter, Saturn, Neptune, and Uranus), or liquid water with ammonia and/or minerals (Europa, Titan, Ganymede, Enceladus, and Mimas). The latter are categorised as icy satellites (or icy moons), a group of natural satellites of the gaseous planets of the Solar System with a near spherical shape, which are mostly made of ice.

Lunine and Stevenson (1987) were the first to predict the presence of a global subsurface ocean on Titan, although it had been suggested by Consolmagno and Lewis (1978). Since then, the presence of an ocean has been supported by several observations and measurements such as Titan's obliquity and mean density (e.g., Baland et al., 2011, 2014), the gravitational tides (e.g., Rappaport et al., 2008; Nimmo and Bills, 2010; Iess et al., 2012), and electric signals (e.g., Béghin et al., 2010; Baland et al., 2014). While the presence of a global subsurface ocean is ascertained, its depth and liquid composition remain open questions. Several models were developed to infer the internal structure of Titan. Using properties such as the second degree tidal Love Number, mean moment of inertia (both were derived by Iess et al., 2012), and the mean density of Titan, Baland et al. (2011, 2014), Fortes et al. (2007), Sohl et al. (2003) and Sohl et al. (2014), among others, were able to constrain the range of profiles predicted. Although different, their results can be used to bound the ocean depth and density: the depth and density range from less than 100 km to 400 km and from 1100 kg/m^3 to 1350 kg/m^3, respectively.[1] The ocean is located between two ice layers: an outer ice shell and a high-pressure ice layer. Depending on the temperature and pressure conditions (and, hence, the model), the crystalline structure of the high-pressure ice is Ice II, Ice III, Ice V, or Ice VI (or a combination of these structures), as detailed in Dunaeva et al. (2016), while the crystalline structure of the outer ice shell is Ice Ih.

Several aspects of the subsurface oceans such as the tidal heating (e.g., Sears, 1995; Sohl et al., 1995; Tyler, 2008, 2009, 2011, 2014, 2020; Chen et al., 2014; Matsuyama, 2014; Beuthe, 2016; Hay and Matsuyama, 2017, 2019; Matsuyama et al., 2018), tidal flow (e.g. Tyler, 2008; Chen et al., 2010), hydrothermal plumes (e.g. Vance and Goodman, 2009; Goodman and Lenferink, 2012), heat transfer and its implication on topography (e.g. Soderlund et al., 2014; Soderlund, 2019; Kvorka et al., 2018), and salinity driven flow (e.g. Kang et al., 2022) were studied. At first, the ocean was considered as a layer among others in studies of the internal structure but, over the last ten years, several studies have focused on the global ocean itself.

Tyler (2008) and Tyler (2009) estimated dissipation in Europa/Enceladus' oceans based on perturbations of inviscid analytical solutions. Tyler (2011) developed a fast, semi-analytical method to take into account strong damping. Using this method to densely sample the domain of tidal solutions, Tyler (2014) provided tidal solutions for the icy satellites oceans, including Titan. The focus was on describing the tidal power (equivalent, by an assumed energy balance, to the average work, dissipation, and heating rate), which can be both low and high for Titan. Tyler (2014) showed that resonant solutions with enough tidal heat to prevent freezing were possible for all ocean thicknesses (i.e. thin oceans are not required for resonant tides). Chen et al. (2014) considered the ocean tidal heating for moons, including Titan, as insignificant. However, this conclusion was drawn without taking into account the influence of the ocean depth on the tidal motion. The ocean component of the model in Beuthe (2016) adopts the same spherical-harmonic formulation and solving method as Tyler (2011) and Tyler (2014) but with extensions to include self-gravity and parameterised effects of the ice membrane. Because the membrane is easily represented by means of spherical-harmonic bases, Beuthe (2016) showed that it could be parameterised within the same formulation but with some of the coefficients reinterpreted or generalised to reflect a dependence on harmonic degree. He concluded that, in Enceladus, energy dissipation mainly takes place in the ice shell, which is forced by the ocean tides, while the dissipation in the ocean is small. Matsuyama (2014) and Matsuyama et al. (2018) also used the same spherical-harmonic formulation and solving method. Matsuyama (2014) studied the tidal dissipation in an ocean covered by a rigid ice shell while taking into account the ocean loading, self-attraction, and the deformation of the bottom of the ocean. These effects increase the resonant depth. The model was improved in Matsuyama et al. (2018) to include a parametrisation of the ice shell effect differing from that of Beuthe (2016): the dynamic part of the ocean forcing on the shell is modelled by a pressure potential, which is rewritten as a function of the surface elevation, tidal potential, and tidal and pressure displacement Love numbers.

In parallel, Hay and Matsuyama (2017) created a numerical model solving the Laplace tidal equations by means of a finite difference scheme to simulate the tidal flow of a global free-surface ocean and predicted the energy dissipated for various depth and various linear and quadratic drag terms. This model was then improved by Hay and Matsuyama (2019) to take into account the ice shell lying above the ocean by means of the same method as that of Matsuyama et al. (2018). They solved the Laplace tidal equation using a numerical model based on a finite volume method. They concluded that the ice shell has little impact on the flow, unlike the self-gravity, which increases the response and dissipation.

In Tyler's initial semi-analytical method (Tyler, 2011, 2014) and in Matsuyama (2014), Matsuyama et al. (2018), Beuthe (2016), Hay and Matsuyama (2017) and Hay and Matsuyama (2019), the Laplace tidal equations are solved. These equations apply (in Laplace's original work) only to thin, uniform-density oceans, though in the extended interpretation they also apply to stratified oceans having an equivalent-barotropic vertical structure. To allow the more versatile consideration of thick, stratified, compressible fluids, a more complete set of equations are solved in the numerical model Tidal Response Of Planetary Fluids (TROPF) (Tyler, 2019, 2020). Similarly to Tyler's previous studies, in attempting to draw robust conclusions despite the large uncertainties in parameters and processes associated with dissipation and ice coupling, Tyler (2020) treated the dissipation and ice as unresolved processes. Instead, they are parameterised generically using free parameters (e.g. the dissipation time scale) which are considered over the full range of plausible values. This more versatile formulation in TROPF also allows more versatile parametrisations of dissipation processes and effects due to ice.

The models developed to study the global subsurface ocean can be differentiated depending on the discretisation. The models of Chen et al. (2014) and Hay and Matsuyama (2017, 2019) are based on discretisations with local bases (e.g. the equations are solved by means of finite-difference or finite-volume methods) while Tyler (2011, 2014, 2020), Matsuyama (2014), Matsuyama et al. (2018) and Beuthe (2016)'s models are based on a discretisation with nonlocal bases (they use a spherical-harmonic formulation and solving method). The latter models are well suited to build solution domains considering the full range of plausible values for the poorly constrained parameters but lack flexibility as these parameters have to be uniform and constant.[2]

[1] The density upper bound is far from the density of an ocean saturated with salts/ammonia dissolved in the water. Such large densities would not be coherent with respect to the observed characteristics (such as the mean density and the Love numbers).

[2] While spherical-harmonic decomposition method allows for non-uniform parameters, the spherical harmonic approach used in these studies does not include orders other than that of the forcing. So this approach cannot be easily extended for non-uniform parameters that vary with longitude.

Finite difference/volume/element methods, on the other hand, can easily handle non-uniform and non-constant parameters and are better suited to study non-linear interactions and baroclinic phenomena which are not easily modelled in the frequency domain. These approaches being more costly, they should be used to zoom in on a solution or a subdomain of the large solution domains provided by the nonlocal bases models.

In this article, we numerically study the liquid motion within the global ocean of Titan by means of the state-of-the-art numerical model SLIM (www.climate.be/slim). It was previously used to study the tides of the surface lakes and seas of Titan (Vincent et al., 2016, 2018). SLIM solves either the 2D depth-averaged shallow water equations (see Section 3.2.1, this version is referred to as SLIM2D) or the 3D baroclinic hydrostatic equations under the Boussinesq approximation (see Section 3.2.2, this version is referred to as SLIM3D). SLIM solves these equations by means of the discontinuous Galerkin finite element method, which makes it a model of the same group as Chen et al. (2014) and Hay and Matsuyama (2017, 2019). We take advantage of the solution domains built by means of TROPF (Tyler, 2019) to focus on specific configurations while taking into account non-linear interactions and 3D circulation. The tidal motion in the global subsurface ocean of the icy satellites can be differentiated between the Europa tidal scenario and the Enceladus tidal scenario. The former is a moon whose obliquity is appreciable while the latter is a moon whose obliquity is several orders of magnitude smaller and whose ocean and ice shell are shallower/thinner. Titan is expected to have a thick ocean and has an appreciable obliquity that was inferred from observation (unlike Europa's obliquity that was theoretically estimated). For this reason, the tidal scenario is expected to be close to Europa's. However, the ice shell thickness may be much thicker than Europa's and not as easily parameterised as in Tyler (2008). More sophisticated ice models should thus be considered. The tidal scenario is investigated by means of SLIM2D, which is also used to conduct a sensitivity analysis with respect to poorly constrained parameters such as the depth of the ocean and the mechanical characteristics of the ice shell. To this end, the model is modified to take into account the influence of the latter on the ocean (see Section 3.2). SLIM3D is used to study the interactions between the tidal flow and the flow induced by the surface heat flux, which was neglected in previous studies. The results can help to further constrain the heat flux and the internal structure of Titan by comparison with observations. Gaining further insight into the flow of a subsurface ocean could also prove helpful for astrobiologists studying the habitability of such oceans.

The article is organised as follows. The internal structure of Titan is briefly described in Section 2 and the model, equations, and boundary conditions are detailed in Section 3 along with the method used to solve the equations on a sphere. In Section 4.2, the tidal response of a free-surface and a subsurface ocean are compared. The liquid motion induced by the surface heat flux is discussed in Section 4.3. A sensitivity analysis with respect to the ocean depth and ice shell mechanical characteristics is then conducted (see Section 5). The results are discussed in Section 6 and conclusions are drawn in Section 7.

2. Computational domain

The internal structure of Titan has been widely studied. The general consensus is a structure consisting of a core, a high-pressure ice layer, a global subsurface ocean filled with liquid water, and an outer ice shell. The composition and thickness of each layer is open to debate as no direct measurements are available to determine them accurately. Indeed, up to now, most of the data constraining the internal layers are provided by means of numerical models based on thermodynamics or solid mechanics laws. These models are validated by comparison with properties inferred from Cassini measurements such as the mean moment of inertia, the second-degree gravity field coefficients, and Titan's mean density. Using models to derive the internal structure of Titan results in uncertainties in the composition and thickness of each layer. Depending on the model and the data used for its validation, the results vary significantly, both in terms of layer configuration and combination of these configurations. The configurations predicted for each layer are briefly introduced hereafter:

- **Core:** Three compositions can be found in the literature (1) a mixture of rock and iron (e.g. Sohl et al., 2003, 2014; Nimmo and Bills, 2010; Baland et al., 2014; Lefevre et al., 2014), (2) silicates (e.g. Fortes et al., 2007; Fortes, 2012; O'Rourke and Stevenson, 2014; Tobie et al., 2012; Castillo-Rogez and Lunine, 2010), and (3) a mixture of rock and water– ice (e.g. Baland et al., 2011).
- **Mantle:** Most models agree on the presence of an ice-rock mantle at the top of the core but differ about its thickness and composition.
- **High pressure ice:** A few models considered a uniform water–ice shell lying beyond the mantle but this was later ruled out (e.g. Sohl et al., 1995; Barr et al., 2010). Most of the models split this layer into a high-pressure ice(s) layer, a global subsurface ocean and an outer ice shell. Depending on the temperature and pressure conditions (and, hence, the model), the crystalline structure of the high-pressure ice is Ice II, Ice III, Ice V, or Ice VI (or a combination of these structures). An overview table is available in Dunaeva et al. (2016).
- **Global Ocean:** The bulk of the ocean is liquid water in which salts, volatiles and/or ammonia are dissolved. Depending on the model and assumptions, the depth and density of the ocean respectively are found to range from less than 100 km (Baland et al., 2014) to 400 km (Lefevre et al., 2014; Mitri et al., 2014) and from 1100 kg/m^3 (Sohl et al., 2003; Nimmo and Bills, 2010; Fortes, 2012, e.g.) to 1350 kg/m^3 (Mitri et al., 2014; Fortes et al., 2007; Baland et al., 2011).
- **Outer icy crust:** All models predict the crystalline structure of the ice shell to be Ice Ih. Depending on the model, the shell is assumed homogeneous or made of several sub-layers of various mechanical properties. Additional features such as methane clathrates can also be included (e.g. Fortes et al., 2007; Kalousová and Sotin, 2020).

In this article, we consider a thin icy crust lying above a subsurface ocean. The ocean bottom is assumed to be static (i.e., it does not deform). Following this hypothesis, the layers beneath the ocean do not impact the tidal motion. The impact of the ocean floor deformation can be modelled by an attenuation factor, γ_2, multiplying the tidal forcing and whose value depends on the core, mantle, and high pressure ice layer properties. According to Hay and Matsuyama (2017), $\gamma_2 = 0.899$, which is close to 1. The impact of the ocean floor deformation is, hence, small and consists in decreasing the surface elevation (which scales linearly with γ_2) and the flow speed. The impact of the deformation is not taken into account in our simulations and is discussed in Section 6.3. The ocean mean density has little impact on the tidal motion while local variations of the density can generate a liquid motion independent from the tides. Such variations could occur due to spatial variations of the temperature and/or liquid composition induced by the non-uniform upper and bottom heat fluxes and the melting/freezing at the boundaries. The impact of the density variations resulting from the surface heat flux is studied by means of SLIM3D (which takes into account both the density gradient resulting from the temperature and the tidal forcing) but is not taken into account in our study of the tidal motion by means of SLIM2D. The impact of the salinity on the density is not taken into account. This strong hypothesis is discussed in Section 6.5.

3. Method

While, in terrestrial atmospheric studies, numerical models have included discretisations with both local (e.g. finite-difference/element/

volume) and nonlocal (e.g. spherical-harmonic) bases, in oceanography the nonlocal bases have been less appropriate because of the lateral boundaries of the ocean and the need to accurately represent local features such as the coastlines and the bathymetry variations. For the spherical oceans in planetary applications, however, Tyler (2011) resorted to a spherical-harmonic base as this allows sampling large solution domains. In this study, the solution domain is sampled by means of TROPF (Tyler, 2019) and a subdomain is then studied by means of a finite-element model, SLIM, as a barotropic (2D) and a baroclinic (3D) version are available. Sensitivity analysis of the tidal motion with respect to poorly constrained parameters are conducted by means of the 2D version, as it is faster than the 3D version and well-suited for barotropic phenomena, while the baroclinic phenomena are modelled by means of the 3D version of SLIM. Both versions allow local variations in parameters and the so-called pole singularity issue is fully circumvented.

In this section, we introduce the main modifications implemented in SLIM (for further details about SLIM, the reader is referred to Kärnä et al., 2013; Vincent et al., 2016). A projection of the whole domain in 2D using a map projection being deemed inappropriate, the model is modified to solve the equations on a spherical mesh (see Section 3.1). The equations solved in the standard version of SLIM are formally valid only for an ocean with a free surface. As in terrestrial oceanography as well as the Tyler studies, the effects of the ice following some ice model assumptions can, however, be parameterised by reinterpreting terms and coefficients already present in the SLIM equations. In order to allow more general ice descriptions to be parameterised, some modifications of the equations were performed (see Section 3.2), which affect both SLIM2D and SLIM3D. The boundary and initial conditions implemented for the temperature equation as part of the study of the surface heat flux influence on the liquid motion are introduced in Section 3.2.3.

3.1. Ocean discretisation

The current version of SLIM is based on the Discontinuous Galerkin Finite Element Method (DGFEM) which solves the equations on a mesh made of triangular (in 2D) or prismatic (in 3D) elements whose size can vary in space. In this study, the length of the sides of the triangles ranges from 59 km to 136 km (the mean length is 64 km). In order to perfectly model a spherical domain, the elements should be spherical triangles. Nevertheless, it significantly increases the numerical complexity (for instance, the mapping with the parent element is no longer linear) and SLIM is not able to use such elements. According to Comblen et al. (2009), the error induced by the use of flat triangles decreases at the same rate as the discretisation error rate when the resolution is increased. Therefore, flat triangular elements are used. The unstructured meshes are generated by means of GMSH (Geuzaine and Remacle, 2009, http://geuz.org/gmsh/).

Various methods allowing to solve equations on a sphere can be found in the literature. We selected the approach developed by Comblen et al. (2009) as it was developed for DGFEM. The original idea is quite simple: in order to solve an equation on a surface, the outgoing flux at the boundary of an element has to be redirected in the tangent plane of the neighbouring element. The method thus takes advantage of the geometrical flexibility inherent to the finite element method to compute the outgoing flux by means of a dialogue between a local coordinate system and an edge-associated one. This approach was developed for 2D flat triangles, which is well-suited for a 2D model such as SLIM2D. On the other hand, a 3D model requires a 3D discretisation of the domain which, in this case, is made of prismatic elements. For each layer of the 3D mesh (i.e. on each triangular face of the prism), the outgoing horizontal flux at the boundary is redirected in the tangent plane of the neighbouring element of the same layer (i.e. in the tangent plane of the adjacent triangular face).

3.2. Dynamical equations under a viscoelastic ice shell

First, we ensure the governing equations of SLIM2D and SLIM3D are well suited to model the liquid motion within the global subsurface ocean. The water density is a function of the water salinity[3] and temperature. Temperature variations are due to the bottom and surface heat fluxes while melting and freezing would modify the salinity by the influx/withdrawal of fresh water. The density variations induced by the temperature are expected to be small with respect to the mean density of the ocean (about 1200 kg/m^3). On the other hand, melting and freezing could locally modify the density by the influx/withdrawal of fresh water whose density could be significantly smaller than the water density, depending on the ice composition. Nevertheless, in this study, the melting/freezing is not taken into account. This strong hypothesis is latter discuss in Section 6.4. The Boussinesq approximation is therefore valid as part of this work. The governing equations also rely on the assumption that the ocean is in hydrostatic equilibrium. This assumption is valid if the aspect ratio is small. Titan's radius and the ocean depth being about 2575 km (from which the surface ice shell thickness has to be deducted) and $\mathcal{O}(100)$ km, the resulting aspect ratio ranges from 0.019 for a 50 km deep ocean to 0.16 for an ocean depth of 400 km. Most of the neglected terms are of the order of the square of the aspect ratio (Cushman-Roisin and Beckers, 2011). Therefore, we deem the aspect ratio small enough to consider the ocean to be in hydrostatic equilibrium when studying the tidal motion. The ocean being heated at the bottom and cooled down at the surface, convection is expected to take place. Such a phenomenon cannot be properly resolved by hydrostatic equations such as those implemented in SLIM. A convective adjustment such as the one proposed by Marotzke (1991) is therefore implemented. It consists in locally increasing the vertical diffusivity to 1 m^2/s where there is static instability (i.e. where Richardson's number is negative). This allows for parametrising the impact of convection in the model. With these assumptions, SLIM2D and SLIM3D can be used to study the liquid motion of a global ocean.

The equations implemented in SLIM are then modified to take into account the impact of the ice shell deformation on the liquid motion, while the deformations of the core and mantle of the moon are neglected (i.e. the bottom of the ocean is assumed to be rigid). The upper shell influences the liquid motion in two major ways: friction takes place at the top of the ocean, and the ice shell vertical deformation results in a surface pressure pushing/sucking the water. The surface pressure acting on Titan's subsurface ocean is derived from an analogy with the simplified case of a spherical shell under internal pressure. In this case, the main stresses are circumferential and there is no shear stress. The circumferential stresses can be related to the internal pressure by computing the force equilibrium on one half of the sphere while the circumferential strains are a function of the radial displacement. The shell being assumed to behave as a viscoelastic material when considering the time and space scales of the main astronomical forcing, the stresses in the shell are assumed to be a function of the strains and strain rates. Using the stress–strain relation and the force equilibrium, the interface pressure can be written as a function of the shell's vertical uplifting and its time derivative. For a motionless ocean, the pressure acting at the surface would therefore be the opposite of the pressure acting on the internal area of the shell. Nevertheless, the ocean experiences its own motion due to the tidal forcing, which attenuates/increases the surface pressure depending on the sign of the difference between the ocean surface elevation and the shell vertical uplifting. The pressure at the ice–ocean interface is thus modelled as a function of this difference instead of the sole shell vertical uplifting. It reads

$$p = a\rho_0 g(\eta - \mathrm{w}_s) + b\rho_0 g \frac{\partial(\eta - \mathrm{w}_s)}{\partial t} \tag{1}$$

[3] The ocean floor is made of ice but a rocky floor was probably exposed in the past and contacts between the ocean and rocks could occur through cracks or through water circulation in the high pressure ice layer. While there may be no salinity (in the sense of terrestrial salinity made of NaCl dissolved in the water) there likely are minerals and/or ammonia playing the same role as the salinity on Earth. Although they play a similar role, their impact on the density cannot be modelled by the equation of state of Jackett et al. (2006).

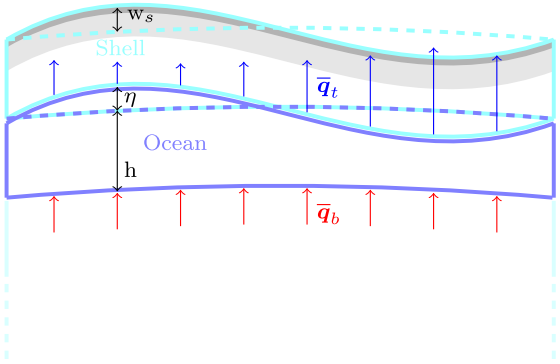

Fig. 1. Geometry of a part of the domain. w_s denotes the vertical displacement of the ice shell (positive upwards), h is the unperturbed ocean depth, η is the surface elevation (positive upwards), $\overline{q}_b$ is the (incoming) uniform heat flux at the bottom of the ocean, and $\overline{q}_t$ is the (outgoing) spatially varying heat flux at the surface of the ocean. Light and dark blue represent the icy parts of the domain and the ocean, respectively. The dashed lines represent the unperturbed ocean/shell. The dark and light grey areas at the top of the ice shell represents the shell upper layer (which is assumed elastic and conductive) for a relative thickness of 10% and 40% of the ice shell, respectively. The shell lower layer (not colourised) is assumed to be convective and elastic-like, viscoelastic, or fluid-like depending on the viscosity ratio. (For interpretation of the references to colour in this figure legend, the reader is referred to the web version of this article.)

where ρ_0 is the reference density, η is the ocean surface elevation (positive upward), w_s is the vertical displacement of the ice shell (positive upwards) (see Fig. 1), and a and b are phenomenological coefficients. In this case, the ocean pushes on the shell if the tidal bulge is larger than the uplifting of the shell and vice versa. Various approaches are available to model the shell deformation. Our approach is based on the membrane theory developed by Beuthe (2015b,a). This is a particular case of the thin shell theory which is appropriate for loads of large wavelength with respect to the shell thickness. This theory relies on assumptions, such as the spherical symmetry for the density and viscoelastic properties of the ice, which might be violated but the theory is satisfactory and well-suited for modelling the shell vertical uplifting. Beuthe derived two approaches: the massless approach (Beuthe, 2015b) and the massive approach (Beuthe, 2015a). The first approach applies for a membrane (i.e. a shell of vanishing thickness) whose density is the same as the ocean's, which, in the model derived by Beuthe (2015b), is equivalent to assuming a massless membrane, hence its name. Following this approach, the uplifting of the ice shell can be related to the ocean elevation by the membrane spring constant (Λ): $\eta = (1+\Lambda)w_s$. The assumptions of a zero thickness membrane with no density contrast with the ocean are not made in the massive membrane approach, which predicts a similar relation with additional terms: the compressibility correction, which vanishes if the crust is incompressible, the minor density correction, which vanishes if there is no density contrast between the shell and the ocean, and the dynamical correction term, which vanishes in the static limit. The membrane spring constant is generally dominant (Beuthe, 2015a), which is why the effects of the ice shell are modelled in SLIM by means of a parametrisation based on the massless membrane approach developed by Beuthe (2015b). The membrane spring constant varies with the ice shell rheology and the shell and its sublayers' thickness. These characteristics are assumed to be longitude and latitude independent, resulting in a uniform membrane spring constant. Λ also varies from one spherical-harmonic component to another. For a deformation of degree n, the membrane spring constant is given by (Beuthe, 2015b)

$$\Lambda_n = 2(n-1)(n+2)\frac{1+\overline{\nu}}{(n-1)(n+2)+1+\overline{\nu}}\frac{\overline{\mu}}{\rho_0\, g R}\frac{d}{R} \tag{2}$$

where $\overline{\nu}$ is the effective Poisson's ratio, $\overline{\mu}$ is the effective shear modulus, d is the ice shell thickness, and R is Titan's radius.

In this article, the solution is computed in the time domain. The spherical-harmonic expansion of the surface elevation should therefore be computed at each time step and each harmonic should then be associated with the corresponding value of the membrane spring constant. Nevertheless, because of the ice rigidity, it is expected that tidal deformation of the shell will be active only at the largest scales and the large scales are dominant in the surface elevation field of a free-surface ocean. For instance, in a free-surface ocean, the decomposition in spherical harmonics of the ocean surface elevation resulting from the tidal forcing results in coefficients of degree 2 which are five orders of magnitude larger than the others (see Fig. 2). The variation of the membrane spring constant with respect to the harmonic degree being small (see Fig. 2), only the degree-two component of the membrane spring constant is computed and η is multiplied by Λ_2 without discriminating the harmonic components. Approximating the membrane spring constant by its degree-two component is equivalent to representing the slowness parameter of Tyler (2020) as a complex constant, in which case the ice damping of the ocean tides is equivalent to a dissipation term in the tidal equations that is proportional to the flow potential energy. For an elastic rheology, $\overline{\nu} = \nu_E = 0.33$ and $\overline{\mu} = \mu_E = 3.5$ GPa (Beuthe, 2015b), which results in a membrane spring constant $\Lambda = \Lambda_2 = 0.055$. For a viscoelastic rheology, the effective Poisson's ratio and the effective shear modulus are complex and their values can slightly vary with the configuration taken into account. In this article, their values correspond to the published results of Beuthe (2015b) and Beuthe (2015a) which are obtained for a specific configuration: Titan is represented by a three-layer incompressible spherical body made of an infinitely rigid mantle, a subsurface ocean, and an ice shell which is itself made of two uniform layers (see Fig. 1). The shell upper layer is assumed to be conductive and elastic whereas its lower layer is assumed to be convective and viscoelastic. In this case, Λ is a function of the relative thickness of the shell upper layer and the ratio, δ, between the critical viscosity and the viscosity of the shell lower layer. Based on the relation between the ocean surface elevation and the shell radial deformation predicted by the massless membrane approach, w_s is rewritten as $\frac{\eta}{1+\Lambda}$ in Eq. (1). In this work, the equations are solved in the time domain, the terms must thus be real. Therefore, only the real part of the surface pressure is taken into account. It reads

$$p = \rho_0\, g A\eta + \rho_0\, g B\frac{\partial \eta}{\partial t} \tag{3}$$

where $A = \frac{\Lambda_r^2+\Lambda_r+\Lambda_i^2}{(1+\Lambda_r)^2+\Lambda_i^2}a$ and $B = \frac{\Lambda_i}{(1+\Lambda_r)^2+\Lambda_i^2}b$ are real parameters quantifying the elastic and viscous deformations of the ice shell. These parameters are function of both the real (denoted by a subscript r) and imaginary (denoted by a subscript i) part of the membrane spring constant, Λ.

Three mechanical characteristics of the shell lower layer can be considered following the value prescribed for the viscosity ratio, δ: $\delta \leq 0.1$ corresponds to an elastic-like lower layer, $0.1 < \delta < 10$ corresponds to a critical (i.e., viscoelastic) lower layer, and $\delta \geq 10$ corresponds to a fluid-like lower layer. For elastic-like and fluid-like lower layers, B is almost zero and A is constant with respect to δ (see Fig. 3). For a critical viscoelastic lower layer, A decreases with δ while, the closer the viscosity of the lower layer to the critical viscosity, the larger the value of B. Such distinct characteristics could differently impact the tidal motion within the ocean. Therefore three configurations are studied: an elastic-like lower layer ($\delta = 0.1$), a viscoelastic-like lower layer ($\delta = 1$) and a fluid-like ($\delta = 10$) lower layer. For each of these configurations, simulations are run for an elastic upper layer making 10% and 40% of the shell thickness.

While the radial deformation of the shell is dominant, circumferential deformation also takes place. It results in a drag term which is subsumed in the drag coefficient (as in Earth applications). Its effect is studied by varying the friction coefficient. Depending on the direction of the shell circumferential deformation, the shear stress at the boundary is larger (opposite direction with respect to the flow) or smaller

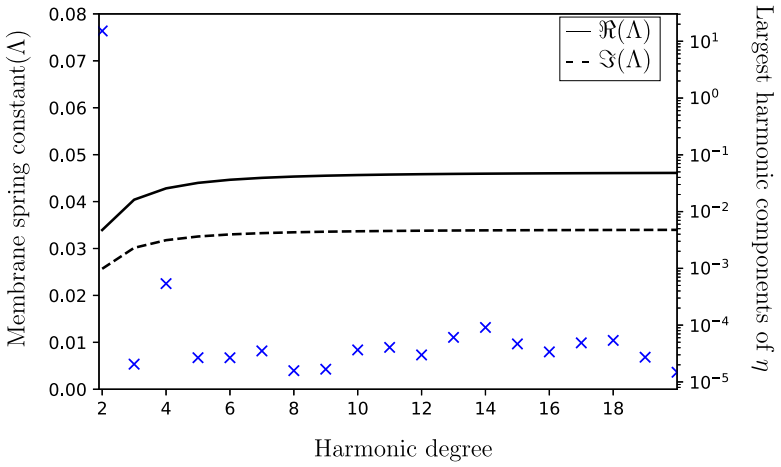

Fig. 2. Real (line) and imaginary (dashed) part of the degree dependent membrane spring constant, Λ, for a 70 km thick viscoelastic ice shell. Both the real and imaginary part increases with the harmonic degree (by about 26% and 23% respectively between degree 2 and 4) and then flattens out for higher degree. For each degree, the magnitude of the largest harmonic component (for all the orders of the degree) is indicated by a blue cross. The degree 2 component is at least five orders of magnitude larger than the others, which is why the Λ_2 is used as an approximation of Λ_n.

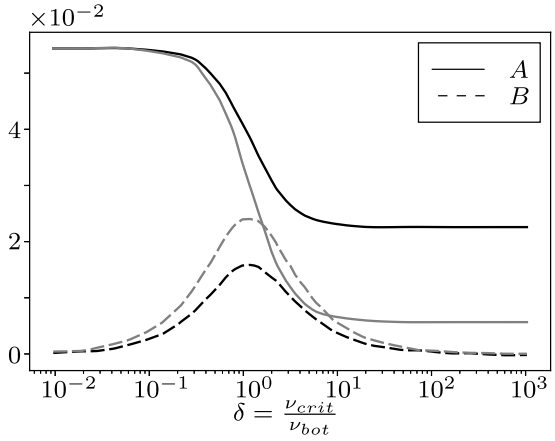

Fig. 3. Real parameters quantifying the impact of the elastic (A, full lines) and viscous (B, dashed lines) deformations of the ice shell in the surface pressure equation. They are computed for a rheology based on Fig. 3 of Beuthe (2015a). Their values depend, among other things, on the relative thickness of the elastic upper layer of the ice shell. The grey and black colours denotes an upper layer representing 10% and 40% of the ice shell thickness, respectively.

(same direction as the flow). Both cases are studied by implementing a larger (resp. smaller) friction coefficient.

The modifications of the shallow water equations are presented in Section 3.2.1 and the corrections of the 3D baroclinic hydrostatic equations under the Boussinesq approximation are introduced in Section 3.2.2. These equations allow studying the impact of the surface heat flux on the liquid motion. To this end, boundary and initial conditions for the temperature equation are needed. They are described in Section 3.2.3.

3.2.1. Shallow water equations

Introducing the surface pressure term in the shallow water equations yields

$$\begin{cases} \dfrac{\partial \overline{\boldsymbol{u}}}{\partial t} + \overline{\boldsymbol{u}}\cdot\nabla\overline{\boldsymbol{u}} + f\boldsymbol{e}_z\wedge\overline{\boldsymbol{u}} + g\nabla\left((1+A)\eta + B\dfrac{\partial\eta}{\partial t}\right) \\ \qquad = \dfrac{1}{H}\nabla\cdot\left(H\nu_h\nabla\overline{\boldsymbol{u}}\right) - \dfrac{\boldsymbol{\tau}^s+\boldsymbol{\tau}^b}{\rho_0 H} + \gamma_2\boldsymbol{S} \qquad (4.1) \\ \dfrac{\partial\eta}{\partial t} + \nabla\cdot\left(H\overline{\boldsymbol{u}}\right) = 0 \qquad (4.2) \end{cases} \qquad (4)$$

where $\overline{\boldsymbol{u}}$ is the depth-averaged velocity; ∇ is the horizontal del operator; $f = 2\Omega\sin\phi$ is the Coriolis parameter ($\Omega = 4.5601\times10^{-6}$ s^{-1} is Titan's orbital angular velocity and ϕ is the latitude); $\boldsymbol{e}_z$ is a unit vector pointing upwards in the local non-inertial Cartesian basis; $H = h+\eta$ is the total liquid depth of the ocean where h is the reference height of the water column; ν_h is the horizontal eddy viscosity; $\boldsymbol{\tau}^s$ is the surface stress; $\boldsymbol{\tau}^b$ is the bottom stress; and $\gamma_2\boldsymbol{S}$ is the astronomical forcing term. The time derivative of the ocean surface elevation, $\frac{\partial\eta}{\partial t}$, in Eq. 5.1 is not computed explicitly, it is replaced by $-\nabla\cdot(H\overline{\boldsymbol{u}})$ for implementation reasons.

Eddy viscosity and friction in the shallow water equations respectively are parameterised by means of Smagorinsky's closure model (Smagorinsky, 1963) and an empirical Earth-based formula. Smagorinsky's closure model is used to account for the kinetic energy dissipated at spatial scales too small to be captured by our model. It is then a function of the local grid size and strain rate tensor. The formulation used to model the bottom and surface stresses is commonly used on Earth. While Titan is a different environment (in terms of temperature, density, and pressure), there is no evidence pointing towards a significant modification of the phenomenological laws representing turbulent flows. Consequently, the same approach as on Earth is implemented: the effect of a turbulent boundary layer at the bottom/top of the ocean is modelled by means of a quadratic drag formulation:

$$\boldsymbol{\tau} = C_D\rho_0|\overline{\boldsymbol{u}}|\overline{\boldsymbol{u}} \qquad (5)$$

where $C_D = 2.5\times10^{-3}$ is the drag coefficient. The same formulation being used for the surface and bottom stresses, their contribution can be summed, which is the same as summing the friction coefficients, which results in $C_D = 5\times10^{-3}$ for a subsurface ocean. While there is no reason to question the quadratic drag formulation, the value of the drag coefficient was derived for Earth oceans and could slightly differ on Titan. Therefore, a sensitivity analysis with respect to this parameter is conducted in Section 5.2.

As described in Tyler (2019, 2020), the effects of the membrane parametrisation in the shallow water equations can already be anticipated by recasting the terms in which they appear to familiar forms. Defining $\eta' = \left[1 + A + B\frac{\partial}{\partial t}\right]\eta$, the last term in the left part of Eq. (4).1 can be rewritten following the conventional pressure-gradient form. The continuity equation (Eq. (4).2) is then altered to the form:

$$\frac{\partial\eta'}{\partial t} + \left[1 + A + B\frac{\partial}{\partial t}\right]\nabla\cdot[H\overline{\mathbf{u}}] = 0. \qquad (6)$$

One immediately sees that the effect of the ice parameter A is to simply increase the effective thickness H. The effect of B is to cause oscillations of η' to experience damping. In the frequency-domain where the

operator $\frac{\partial}{\partial t}$ can be replaced by an imaginary constant, the combined effects of the ice can be understood as simply replacing the squared wave speed gH (or its inverse, the slowness parameter) with a complex constant. Looking at the adjustments to the conventional equations, it is clear that there are two physical effects of the ice on the ocean: an increase of the effective wave speed, and a damping of the vertical motion.

3.2.2. Baroclinic equations

The surface pressure term is the same as in the depth-averaged model, resulting in a similar modification of the momentum equation. The 3D hydrostatic equations under the Boussinesq approximation then read:

$$\begin{cases} \dfrac{\partial \boldsymbol{u}}{\partial t} & + & \nabla_h \cdot (\boldsymbol{u}\boldsymbol{u} + \dfrac{\partial w\boldsymbol{u}}{\partial z}) = -f\boldsymbol{e}_z \wedge \boldsymbol{u} - \dfrac{g}{\rho_0}\nabla_h \displaystyle\int_h^\eta \rho' d\zeta \\ & - & g\nabla_h \left((1+A)\eta + B\dfrac{\partial \eta}{\partial t} \right) \\ & + & \nabla_h \cdot (\nu_h \nabla_h \boldsymbol{u}) + \dfrac{\partial}{\partial z}\left(\nu \dfrac{\partial \boldsymbol{u}}{\partial z}\right) + \gamma_2 \boldsymbol{S} \\ \dfrac{\partial \eta}{\partial t} & + & \nabla \cdot \left(H\bar{\boldsymbol{u}}\right) = 0 \\ \nabla_h \cdot \boldsymbol{u} & + & \dfrac{\partial w}{\partial z} = 0 \\ \dfrac{\partial T}{\partial t} & + & \nabla_h \cdot (\boldsymbol{u}T) + \dfrac{\partial (wT)}{\partial z} = \nabla_h \cdot (\kappa_h \nabla_h T) + \dfrac{\partial}{\partial z}\left(\kappa \dfrac{\partial T}{\partial z}\right) \end{cases} \tag{7}$$

where T is the temperature field, $\boldsymbol{u}$ is the horizontal velocity, w is the vertical velocity, $\rho' = \rho - \rho_0$ is the density deviation with respect to the reference value, ν and ν_h are the vertical and horizontal eddy viscosities and κ and κ_h are the vertical and horizontal diffusivities. The horizontal eddy viscosity is given by Smagorinsky's closure model (Smagorinsky, 1963) which is a function of the local grid size and horizontal strain rate tensor. The vertical eddy viscosity and diffusivity are determined by the Pacanowski–Philander closure scheme (Pacanowski and Philander, 1981), except where there is static instability (i.e. where Richardson's number is negative), in which case the vertical diffusivity is increased to 1 m^2/s following the convective adjustment proposed by Marotzke (1991). The temperature field varying spatially and temporally, it is simulated by an advection–diffusion equation where the horizontal eddy diffusivity is evaluated by Okubo's formula (Okubo, 1971). The relevant initial and boundary conditions are described in Section 3.2.3.

In numerous oceanic model, the density is a function of the temperature and salinity following the equation of state of Jackett et al. (2006). Due to the lack of information about the "salinity" field in Titan's ocean, the salinity equation is disregarded and the density is derived from the sole temperature field. The influence of the temperature on the density is therefore modelled by a linearisation of Kell (1975)'s formulation near a temperature of $T_0 = 282.75$ K: $\rho = \rho_0 - 0.096(T - T_0)$. Neglecting the salinity in the ocean is a strong hypothesis which is discussed in Section 6.5.

SLIM3D allows a more realistic treatment of the friction than SLIM2D as boundary conditions consistent with friction are implemented at the top and bottom of the ocean, resulting in distinct boundary layers. In 3D terrestrial domain, the friction coefficient is computed from the inversion of the Prandtl–Karman law of the wall: this law is used to predict the current friction velocity which is then used to compute the friction coefficient corresponding to this velocity (see, e.g., Kärnä et al., 2013, for further details about the implementation). To this end, the user has to provide parameters of the boundary layer such as the bottom roughness length, and the vertical coordinates where the current friction velocity is defined. As such parameters are unknown in Titan's subsurface ocean, the friction coefficients are fixed a priori using the same friction coefficient (2.5×10^{-3}) at the top and bottom of the ocean. Using the same uniform value for the friction coefficients at the top and bottom boundaries is an assumption we made due to the lack of information on how this coefficient would vary. Various phenomena could impact the coefficient value: the physicochemical nature of the water could differ between the top and bottom of the ocean due to the higher pressure, melting and freezing processes could locally modify the roughness of the ice, and the liquid properties could vary due to the temperature and salinity spatial variations, resulting in spatial variations of the boundary layer and, hence, of the friction coefficient. However, small, local, variations of the friction coefficient are not expected to significantly modify the liquid motion (NB: the water density impacts the friction term in the equations, it is the impact on the sole friction coefficient which is disregarded) and using an uniform coefficient is an hypothesis often resorted to in terrestrial domain (except in domain where specific terrain such as mangroves takes place). The impact of the friction coefficient on the tidal motion is briefly studied in Section 5.2 for various uniform friction coefficients (by means of SLIM2D). The impact on the tidal motion being almost insignificant, no further study is conducted.

3.2.3. Initial and boundary conditions for the temperature equation

In order to predict the temperature field, boundary conditions at the top and bottom of the ocean are needed. The upper boundary condition that is implemented is the surface heat flux predicted by Kvorka et al. (2018). They derived the heat flux taking place at the top of the ocean from the topography of Titan by modelling the melting/crystallisation process at the water–ice interface and the resulting mechanical response of the ice shell. They were able to determine the heat flux associated with the large scale processes (small scale processes were disregarded because of the lack of information). The surface heat flux predicted when erosion is neglected is used as surface boundary condition in this work. Using all spherical-harmonics up to degree 6, they predicted a heat flux ranging from less than 2×10^{-3} W/m^2 to more than 10^{-2} W/m^2 (see Fig. 9(b) in Kvorka et al., 2018). The heat flux being a major parameter in this model, a similar simulation using a zonally uniform heat flux is also conducted (see Section 5.4).

According to Choblet et al. (2017), the heat flux at the bottom of the ocean ranges from 5×10^{-3} to 40×10^{-3} W/m^2, depending on the core properties, and varies spatially due to the high pressure ice shell. Indeed, the radiogenic heat flux melts the ice at the bottom of the latter. This water is transported to the ocean by hot convective plume conduit, resulting in a non-uniform bottom heat flux. Conducting a sensitivity analysis with respect to the value and spatial distribution of the bottom heat flux is impossible as there is a large number of configurations and no information available to favour one of them. Therefore, we resort to a good practice that consists in assuming the ocean is in thermal equilibrium. The implemented bottom heat flux is assumed uniform and its value, about 6×10^{-3} W/m^2, is computed such that the surface integral of the incoming flux at the bottom of the ocean is the same as the surface integral of the outgoing flux at its top. This hypothesis is discussed in Section 6.4.

The temperature field resulting from the bottom and surface heat fluxes is not uniform and therefore neither is the density. The timescale associated with the thermally driven flow being much larger than 1 Titan day (TD), we implement initial conditions corresponding to the steady-state solution predicted when the tidal forcing is ignored and the surface and bottom heat fluxes are used as boundary conditions (see Section 4.3). This scenario is referred to as HFNT. Using the predicted steady-state solution as initial condition, simulations of the liquid motion are then conducted by taking into account both the tidal forcing and the bottom and surface heat fluxes. This scenario is referred to as HFWT. The initial temperature field used to compute HFNT is derived from the melting temperature at the bottom of the ocean (281 K). It is assumed to be uniform in the meridional and zonal directions and to vary linearly with depth, the temperature increasing with depth to reach 281 K at the bottom of the ocean. The initial temperature and density fields could be non-uniform in the meridional and zonal directions due to the spatial distribution of a realistic bottom heat

flux.[4] Nevertheless, a uniform bottom heat flux being implemented in this model, the initial temperature and density fields are also assumed uniform.

Our model is sensitive to parameters such as the thickness and rheological properties of the ice shell. Although the derivation of the surface heat flux is based on the fact that the shell thickness can vary spatially, such variations are not taken into account while computing the impact of the shell deformation on the liquid motion. Taking into account such variations would require a much more elaborate model than the membrane approach (which assumes an axisymmetric shell). The thickness variations being small with respect to the shell thickness, at most $\mathcal{O}(200)$ m according to Kvorka et al. (2018), disregarding them while modelling the impact of the shell deformation seems to be a valid simplification.

4. Results

In this section, we first describe the solution domain computed by means of TROPF (see Section 4.1). This approach is to sample and characterise the large solution domain allowed by generic dissipation forms. This is instructive for understanding the range of tidal-response behaviours but it also replaces the need for some sensitivity studies using SLIM, the latter being time consuming. The tidal response of a global ocean where only the well established dissipation processes are included (see Section 4.2.1) are then studied and compared to the Europa tidal scenario. Damping or other effects by ice cover are not represented. It is therefore expected to be a limiting reference case describing a (possibly extreme) underestimate of the dissipation. We refer to this case as FSO100 (an overview of all the scenarii studied and their name is available in Table 1). The impact of the ice shell on the tides is then studied by means of a parametrisation based on the membrane approach (see Section 4.2.2, this case is referred to as SSO110) and the results are compared to the tidal motion of FSO100. Finally, we study the impact of the surface heat flux on the liquid motion of the subsurface ocean (see Section 4.3, this case is referred to as HFWT).

The results are obtained for a 100 km deep ocean. The drag coefficient for a free-surface ocean is $c_D = 2.5 \times 10^{-3}$, which is the value commonly used in Earth-based model. The subsurface ocean of SSO110 lies beneath a viscoelastic ice shell whose elastic upper layer makes 10% of its thickness (see Sections 3.2, 4.2.2). The associated drag coefficient is $c_D = 5 \times 10^{-3}$.

4.1. Solution domain

As described in Tyler (2020), the two important physical effects of the ice expected from terrestrial studies of wave propagation under ice also seem to be the dominant effects in the more complex viscoelastic ice model of Beuthe (2016). These two effects are as follows: first, the ice can damp the response, in a process that involves transfer of energy from the ocean tides to the ice, and ultimately the generation of heat. Second, the rigidity of the ice creates an effective ocean–ice wave mode that propagates faster than the shallow-water wave speed of an ice-free ocean. Because the speed alteration can be scale dependent, this effect can be regarded more generally as dispersion. While both of these effects (attenuation, dispersion) of ice are known from terrestrial oceanography (e.g. Squire et al., 1995; Squire, 2007; Vaughan et al., 2009; Wadhams et al., 1988), the effect on wave speed is generally small. The potentially larger effect for thick ice on cold bodies is therefore a very important new consideration in planetary studies (Beuthe, 2016). Following the precedent in terrestrial oceanography, these cases should be referred to as "ocean" (not "crustal") wave/tidal dissipation because it is the ocean wave energy being lost to work on the ice (ultimately generating heat in the ice or ice/ocean interfacial region). A rather different case where it is the ice that is most excited by the tidal gravity field (and then losing its energy by working on the ocean) seems much less likely given that fluids, by definition, are a medium that responds very readily to forces. Within the wide range of ocean world scenarios that include ice layers much more massive than the fluid layer, such cases of a dominantly crustal tidal response may be possible. Note that previous to the introduction of considering the dynamic ocean tidal response in Tyler (2008), the ice+ocean tidal response could indeed show a massive ice layer as the dominant responder to the tidal forces. But this is because the water ocean layer was allowed no self-consistent dynamics and essentially acted simply as a lubricant decoupling the ice layer. Clearly, in all these cases both the ice and ocean affect the tidal response. But it is important to clarify which is primarily being worked on by the tidal gravitational field to understand the expected transfer of energy and momentum between the ice and ocean. In all of the modelling results presented in this paper, the ocean is dominating the tidal response and so these models can be regarded as ocean tidal models with the ice effects entering as a parameterised process affecting this response.

The solution domains are described in terms of tidal power characterised as a function of the non-dimensional dissipation time scale $\tilde{T}$ and non-dimensional wave speed $\tilde{c_e}$. The information from Figs 16 and C21 in Tyler (2014) are combined here and represented in Fig. 4. While this figure provides power solutions for a wide range of ocean scenarios without requiring explicit prescription of the dissipation process and ice effects, for comparison purposes, the predicted scenarios are interpreted here as involving linearised bottom friction dissipation and an ice-free, uniform ocean. In this case, the non-dimensional dissipation time scale $\tilde{T}$ can be directly associated with the choice of the friction coefficient, and since there is only one dissipation process present, the parameter Q (used in Tyler, 2014) is also uniquely defined and related by $Q = 1/2\tilde{T}$. The wave speed in this case is the barotropic wave speed ($c_e = \sqrt{gh}$) and $\tilde{c_e}$ represents c_e divided by the equatorial rotation speed. With c_e connected to the ocean depth in this way, the limits for the ocean depth between 50 and 400 km require that the solution fall between the dotted green horizontal lines. If the tides generate all of the heat flux within the observationally inferred range described by Kvorka et al. (2018), then the solutions would also fall between the dashed cyan lines. The requirement that the nonlinear drag form is satisfied can be met *a posteriori* using the solutions computed. For a value $C_D = 2.5 \times 10^{-3}$, the solution must fall on the black diagonal curve (other choices of C_D land the solution on one of the dotted black curves). While the dissipation processes in Titan's ocean are not known, it can be assumed that at least there is bottom friction and it seems reasonable to use a bottom friction coefficient whose value is the same as in terrestrial model, as discussed in Section 3.2.2. The black curve then forms a "separatrix" (Tyler, 2014) excluding the solutions to the right of the curve as they are dynamically unattainable for Titan parameters, the dissipation time scale being larger than the largest $\tilde{T}$ expected. Additional dissipation processes would decrease the dissipation time scale, allowing solutions to the left of the curve.

The different tidal-response regimes described in Tyler (2014) are labelled. In the lower right part in Fig. 4, the response is mediated by rotational-gravity waves (i.e. Class I oscillations). These resonance peaks are narrow and strong for the underdamped cases ($\tilde{T} > 1$) but the resonances blend together and extend to higher $\tilde{c}_e^2$ as critical damping ($\tilde{T} = 1$) is approached. On the overdamped side ($\tilde{T} < 1$), power decreases because the increase in dissipation by decreasing $\tilde{T}$ is overcompensated by the loss in kinetic energy due to this damping. Obliquity tidal forces, i.e. the tidal forces arising from the existence of an obliquity, (degree-two, tesseral harmonics) generate the Rossby waves (Class II oscillations) ridge of solutions in the upper right in

[4] The surface heat flux is also responsible for temperature and density variations in these directions. This part of the study aims at predicting the impact of the surface heat flux on the density, which is why a horizontally uniform initial temperature/density is consistent regarding the latter.

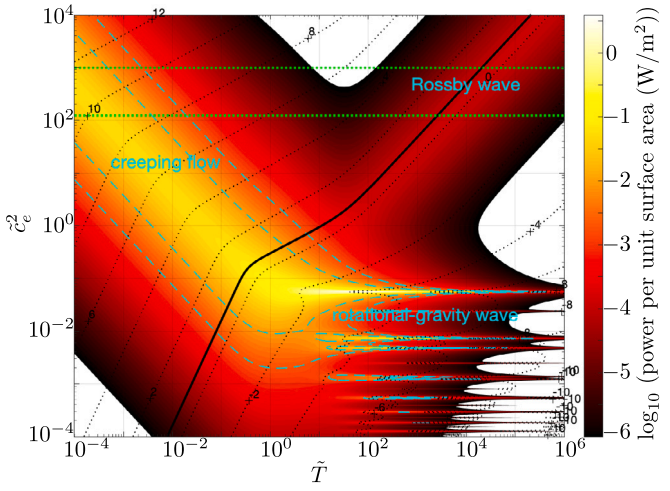

Fig. 4. Tidal power as a function of non-dimensional time scale ($\tilde{T}$) and non-dimensional squared wave speed ($\tilde{c}_e^2$). The dotted green lines are limits for ocean depths between 50 and 400 km while the dashed cyan lines delimit the observationally inferred range described by Kvorka et al. (2018). The black curve correspond to solutions with a quadratic drag formulation whose friction coefficient is $C_D = 2.5 \times 10^{-3}$. (For interpretation of the references to colour in this figure legend, the reader is referred to the web version of this article.)

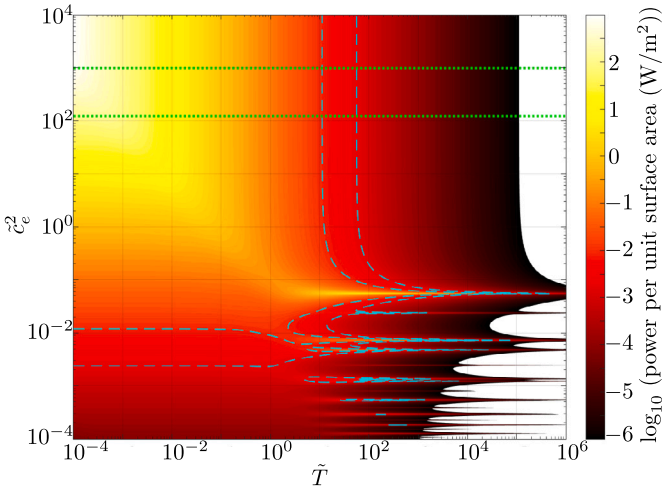

Fig. 5. Tidal power as a function of non-dimensional time scale ($\tilde{T}$) and non-dimensional squared wave speed ($\tilde{c}_e^2$) assuming potential energy is dissipated. The dotted green lines are limits for ocean depths between 50 and 400 km while the dashed cyan lines delimit the observationally inferred range described by Kvorka et al. (2018). (For interpretation of the references to colour in this figure legend, the reader is referred to the web version of this article.)

Fig. 4 (the solution described for Europa in Tyler, 2008, is an example). The underdamped solutions involve minimal vertical flow motion. In the limit of no dissipation, the vertical motion vanishes, leading to a surface elevation equals to the geoid. In this case, there would only be tangential (not normal) stresses with an overlying ice layer and so the damping by ice could be small. The solutions shown in the Rossby regime could remain valid even with ice cover. The same solution set can also describe other model assumptions (including ice cover or stratified oceans) with a reinterpretation of the dimensionless parameters.

The solution domains computed show that the amount of kinetic energy available for dissipation by friction in the ocean can reach up to 10^{-1} W/m^2. As shown in Fig. 4, high-power tidal states do not require shallow oceans: overdamped (creeping flow) solutions and underdamped Rossby solutions are possible. Not only does the figure show that for high-power solutions, one need not have the small $\tilde{c}_2^2$ required for entering the rotational-gravity regime of sharp peaks, it in fact also shows that these resonant, thin-ocean states are forbidden, at least within the barotropic interpretation of the non-dimensional parameters, as they are located to the right of the separatrix. The rotational-gravity regime is indeed reachable under very plausible assumptions when one reinterprets $\tilde{c}_e$ as representing the wave speeds for a stratified ocean (Tyler, 2009, 2011, 2014, 2020).

With a simple reinterpretation of non-dimensional parameters, the solution domain in Fig. 4 does not cover an ocean under the ice membrane model. Indeed, the limitation of this model is that, while the dissipation process is deliberately left unspecified and parameterised through the time scale $\tilde{T}$, it is assumed that the dissipation is coming from the ocean tidal kinetic energy (as is true for drag-law dissipation forms). However, the liquid motion in the ocean results in a work performed by the ocean, on the ice shell, hence inducing a loss of potential energy from the ocean (this energy is transferred to the ice shell). This is referred to as potential energy dissipation in Tyler (2020) and hereafter.[5] This limitation was overcome in Tyler (2020) by including solution domains that draw energy from the ocean tidal potential energy (instead of or in combination with kinetic-energy dissipation). An example of such dissipation in the atmosphere is Newtonian Cooling where vertically propagating waves are attenuated by radiative cooling associated with unresolved processes. An example of such energy loss in the ocean is the representation of the viscoelastic membrane model in Tyler (2020), where it was shown that the effects of the ice could be regarded as damping of vertical ocean motion by an unresolved process having a time scale that could be treated as a free parameter to vary over the full plausible range. In this potential-energy family of energy loss, Fig. 4 is replaced with Fig. 5 (obtained by rescaling the generic solutions in Tyler, 2019). The location of the rotational-gravity regime remains the same, the Rossby regime is masked by the higher power, and the overdamped regime shows a monotonic increase in power levels with decreasing time scale (which must at some point challenge the model assumptions). Fig. 5 shows that the related tidal power can be larger than that associated with kinetic energy dissipation. The sub-domain corresponding to a tidal power equal to observationally inferred range described by Kvorka et al. (2018) and to an ocean whose depth is between 50 and 400 km is associated with a time scale much larger than the one computed for kinetic energy dissipation: it ranges from $\tilde{T} = 10$ to $\tilde{T} = 50$ and from $\tilde{T} = 5 \times 10^{-4}$ to $\tilde{T} = 2 \times 10^{-2}$, respectively.

4.2. Tidal motion

The Rossby and Reynolds number associated with the tidal flow are $\mathcal{O}(10^{-4})$ and $\mathcal{O}(10^{10})$, respectively. These numbers slightly vary with the parameters but by less than one order of magnitude (except between a 400 km deep and a 50 km deep ocean). The Reynolds number is similar to the range observed in Earth's ocean for the M2 tide while the Rossby number is one order of magnitude smaller. It implies that the inertial force is smaller with respect to the Coriolis force on Titan although their ratio with respect to the viscous forces is similar to that observed on Earth. The non-linear terms are therefore small with respect to the Coriolis term. The tidal forces induced by the existence

[5] We did not study the energy dissipation mechanism in the ice shell. Although we refer to this transfer of potential energy to the ice shell as dissipation, this energy could be transferred again from the shell to another part of Titan without being dissipated in the shell but it wille eventually be dissipated somewhere, which is why we refer to it as potential energy dissipation.

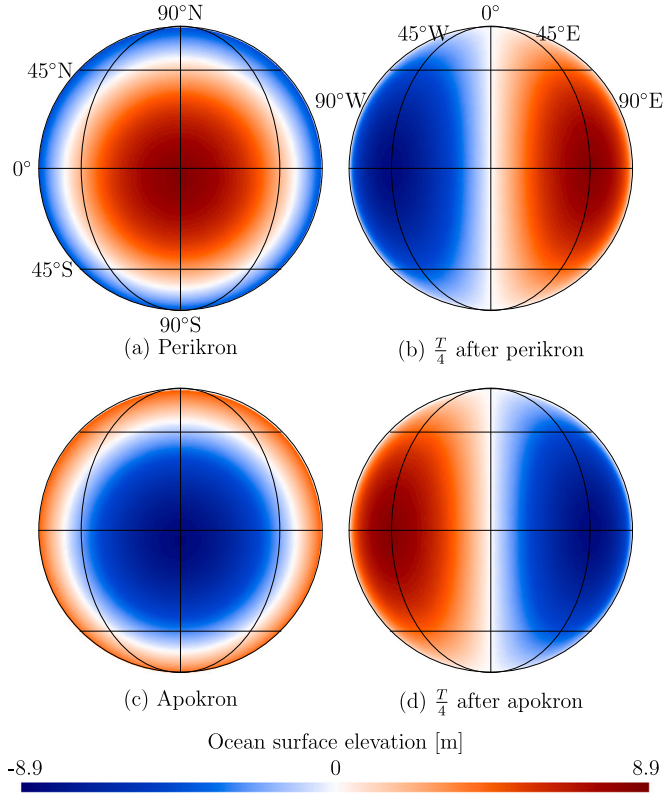

Fig. 6. Elevation field at (a) perikron, (b) 0.25 TD after perikron, (c) apokron, and (d) 0.25 TD after apokron for a 100 km deep free-surface ocean. It consists of two antipodal bulges/troughs rotating eastwards around Titan. The main contribution to the elevation comes from the eccentricity tide while the main impact of the obliquity tide on the elevation consists in moving the bulges/troughs centre away from the equator. (For interpretation of the references to colour in this figure legend, the reader is referred to the web version of this article.)

of an eccentric orbit of Titan around Saturn and by Titan's obliquity, called eccentricity and obliquity tidal forces, are considered together because of the nonlinear terms involving products of the velocities.

4.2.1. Free-surface ocean

The tidal scenario predicted (FSO100) is similar to the Europa tidal scenario described by Tyler (2008) which makes sense as the solution domain for Titan is very similar to that for Europa except that, being more distant from its parent, the amplitudes are smaller (Tyler, 2014). Both the obliquity and orbital eccentricity tidal forces contribute to the tidal motion but their impacts differ: the eccentricity tidal force results in a large surface elevation (at most 8.1 m) associated with a very slow flow (at most 6.6×10^{-4} m/s) while the obliquity tidal force results in small variations of the surface elevation (at most 0.74 m) associated with a much faster flow (at most 1.35×10^{-2} m/s). The spatial distributions of the elevation and depth-averaged velocity fields predicted for both forcings are similar to those predicted by Tyler (2008).

The elevation field mainly consists of two antipodal bulges and two antipodal troughs rotating eastwards around Titan in 2 TD, resulting in a tidal period of 1 TD. These bulges/throughs are not centred on the equator due to the obliquity tidal force (for a 0° obliquity, they would be centred on the equator) but rather on the circumference delimited by (3.22°S, 0°E), (0°S, 90°E), (3.22°N, 180°E) (see Fig. 6). The maximum/minimum elevation, ±8.89 m, is reached in the centre of the bulges/trough 0.165 TD after perikron/apokron.

The main tidal component is the diurnal one, with an associated tidal range of 17.8 m (see Fig. 7). Other components are not significant

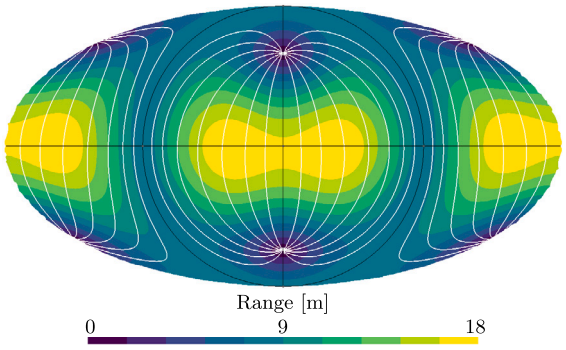

Fig. 7. Tidal range (in m) and phase (white lines, with a 22.5° spacing) of the main tidal component for a 100 km deep free-surface ocean (FSO100) displayed on a Mollweide projection of the sphere. The 90°E and 90°W meridians correspond to a tidal phase of 180°. There are four amphidromic points located at (58.5°N, 180°E), (51.8°S, 180°E), (51.8°N, 0°E), and (58.5°S, 0°E). (For interpretation of the references to colour in this figure legend, the reader is referred to the web version of this article.)

as the tidal range associated with them is, at most, $\mathcal{O}(10^{-4})$ m. A central symmetry with respect to Titan's centre can be observed in the tidal range of the diurnal component. In the hemisphere ranging from 90°W to 90°E, there are two amphidromic points, at (51.8°N, 0°E) and (58.5°S, 0°E), and two local maxima at (1.69°S, 32.2°W) and (2°S, 32.5°E). There is no symmetry with respect to the equator: the southern amphidromic point is located at higher latitudes than the northern one. The amphidromic points locations also influence the shape of the high tidal range area, which spreads further southwards than northwards. This asymmetry with respect to the equator is due to the obliquity tidal force. While the eccentricity tidal force results in a symmetric tidal range, the obliquity tidal force results in a anti-symmetric tidal range. The combination of both forces results in a tidal range which is asymmetric with respect to the equator. Similar patterns can be observed in the other hemisphere, but their location is different: the amphidromic points and the maxima are located at (58.5°N, 180°E), (51.8°S, 180°E), (1.69°N, 147.8°W), and (2°N, 147.5°E), respectively. The tidal phase is also symmetric with respect to the centre of Titan. For the hemispheres centred on the 0° and 180° meridian, the tidal phase is an odd function of the longitude (i.e. the phase at longitude $\lambda_{ref} + \lambda$ is the opposite of the phase at a longitude $\lambda_{ref} - \lambda$, where λ_{ref} is the longitude of the meridian at the centre of the hemisphere). The tidal phase of the circle formed by the 90°E and 90°W meridians, which corresponds to a ring of constant tidal range, is 180°. It is negative from 0°W to 90°E and from 90°W to 180°W.

The depth-averaged velocity field can be seen as the motion of an ocean rotating as a solid body with its pole displaced from the body's spin pole and precessing once a day. In the frame of the body, it appears as an ocean in solid rotation around a pole that progresses westward along the equator. The depth-averaged velocity field consists of two antipodal gyres separated by a ring of unidirectional high speed flow (see Fig. 8). The water rotates clockwise in one of the gyres and anticlockwise in the other so that the ring of high speed flow is a prolongation of each gyre. The gyres move westward with their centre following a sinusoidal path of small amplitude around the equator. For instance, at perikron, the gyres are centred at (2.53°S, 107°E) and (2.23°N, 73°W), which is slightly after a local extrema of the sinusoid. The wavelength of the sinusoidal path is equal to one third of Titan's diameter and it takes 1 TD for each gyre to turn around Titan. The maximum depth-averaged speed is 1.35×10^{-2} m/s, which is two orders of magnitude larger than that observed in the gyres, and changes by less than 2×10^{-4} m/s over the whole tidal period. In the gyres, the depth-averaged speed is slower than 5×10^{-4} m/s and decreases towards their centre. The obliquity tidal force is responsible for a

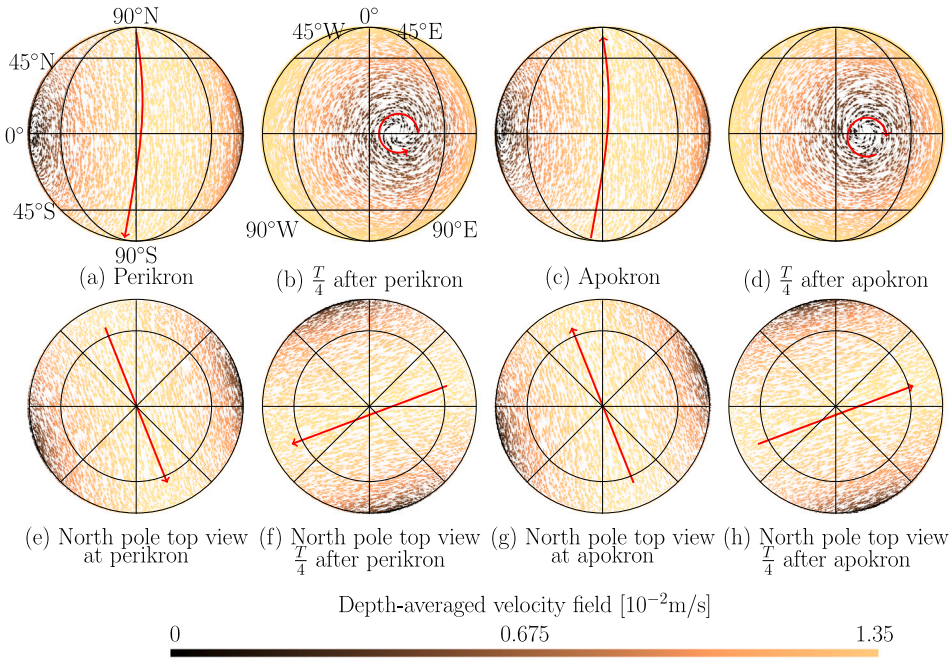

Fig. 8. Depth-averaged velocity field at (a, e) perikron, (b, f) 0.25 TD after perikron, (c, g) apokron, and (d, h) 0.25 TD after apokron for a 100 km deep free-surface ocean. For Panels (a), (b), (c), and (d) the north/south pole is at the top/bottom of the image, which is centred on the 0° meridian. Panels (e), (f), (g), and (h) correspond to an upper view of the north pole with the 0° meridian at the bottom of the image. The meridians/parallels are represented in black, with a 45° spacing. The global direction of the depth-averaged velocity field is marked by red arrows. The depth-averaged velocity field can be seen as the motion of an ocean rotating as a solid body with its pole displaced from the body's spin pole and precessing once a day. (For interpretation of the references to colour in this figure legend, the reader is referred to the web version of this article.)

fast ($\mathcal{O}(10^{-2})$ m/s), mainly divergence-free, component of the depth-averaged velocity field while the eccentricity tidal force results in a slow ($\mathcal{O}(10^{-4})$ m/s), strongly divergent component and is responsible for the gyres' centre following a sinusoidal path centred on the equator instead of an equatorial path. The obliquity tidal force will, hence, mainly lead to kinetic energy dissipation by friction at the boundaries of the ocean while the eccentricity tidal force is mainly responsible for storing potential energy in the ocean.

4.2.2. Subsurface ocean

In the previous section, we studied the tidal motion of a free-surface ocean (FSO100). Nevertheless, the global ocean observed on Titan lies beneath an ice shell. Therefore, in this section, the liquid motion of a 100 km deep ocean lying beneath a 70 km thick shell whose upper layer represents 10% of its thickness and whose lower layer is at the critical state (i.e. $\delta = 1$ in Fig. 3) is studied (SSO110). This configuration results in A and B factors (see Eq. (3)) of the same order of magnitude, meaning that the elastic and viscous deformations are equally significant. The liquid motion predicted is compared to that of a 100 km deep free-surface ocean to highlight the impact of the ice shell on the tidal motion.

The impact of the ice shell on the elevation and depth-averaged velocity fields is noticeable: it damps the tidal motion, resulting in a smaller surface elevation and a slower flow, but the global patterns of these fields are similar. The larger speed difference (7.16×10^{-4} m/s, which represents 5.3% of the depth-averaged velocity at this location) occurs when and where the depth-averaged speed is maximum. The difference between the elevation of FSO100 and that of SSO110 consists of two bulges/troughs rotating around Titan. This field ranges from −0.29 to 0.29 m. The difference is negative/positive where the elevation is negative/positive and the larger the amplitude of the elevation, the larger the difference. The smaller elevation amplitude integrally results from the diurnal tidal component whose range diminishes by 0.58 m. The phase of the diurnal component vary by less than 0.05°.

The tidal scenario for a subsurface ocean is therefore similar to that of the free-surface ocean, although the amplitude of the elevation and depth-averaged velocity fields are slightly smaller. Therefore, the Europa tidal scenario still holds for a subsurface ocean, suggesting the simple analytical solution to the tidal response in Tyler (2008) may be a good first description of the tidal response on many bodies with thick oceans under ice.

4.3. Thermally driven flow

Spatially varying bottom/surface heat fluxes can generate a significant motion in a liquid body (e.g., Goodman and Lenferink, 2012; Zhu et al., 2017; Soderlund, 2019). We therefore study the impact of the surface heat flux derived by Kvorka et al. (2018) on the liquid motion in Titan's ocean. To this end, SLIM3D is used to solve the 3D baroclinic hydrostatic equations under the Boussinesq approximation while taking into account the impact of the temperature on the density field and using a convective adjustment. We first describe the steady-state solution (HFNT) used as initial condition. The interactions with the tidal flow are then highlighted by comparing HFWT with SSO110.

The steady-state results of HFNT are obtained in an ocean where the only forcings taken into account are the constant heat flux at the top and bottom boundaries. While the water is initially warmer at the bottom of the ocean, this changes with time as the water mixes and the temperature tends to uniformity. The vertical structure of the temperature reaches an unexpected configuration: the temperature decreases with depth (see Fig. 9(a)). Although the difference between the maximum and minimum temperature is small (0.31 K), a thin layer of warmer water was expected to be found at the bottom of the ocean, as predicted by the convection models (see Amit et al., 2019; Soderlund, 2019; Kang et al., 2022; Zeng and Jansen, 2021). The warm water seems to be transported away and mixed too quickly to be able to form such a layer. In this case, the larger mixing would have the impact of decreasing the temperature gradient and hence slowing down the thermally driven circulation while still capturing its global patterns. Zonal and meridional variations of the temperature take place at each depth but they are much smaller (a few hundredth of degree) than the vertical variations. The zonally averaged zonal flow differs significantly

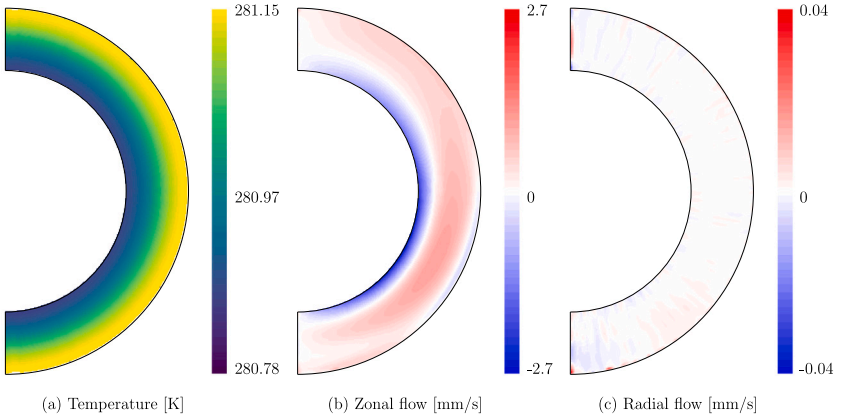

Fig. 9. Zonally averaged temperature field (a), zonal flow (b), and radial flow (c). The radial direction is not to scale for visualisation purpose. The temperature increase towards the surface once the temperature-driven flow is well established. The radial flow is slow (less than 0.04 mm/s) and is much larger near the surface. The zonal heat flux changes of direction with the depth and is twice stronger at the bottom of the ocean. (For interpretation of the references to colour in this figure legend, the reader is referred to the web version of this article.)

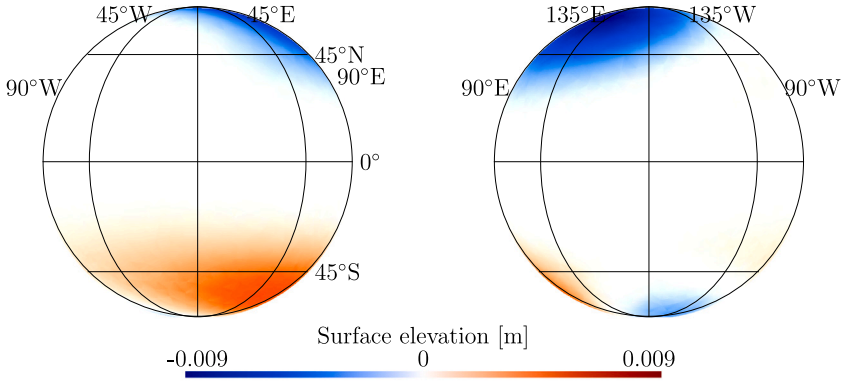

Fig. 10. Ocean surface elevation generated by the heat flux predicted by Kvorka et al. (2018). It is at rest over most of the ocean, positive near the south pole and negative near the north pole and in a small area near the south pole. The area where the ocean surface elevation is positive is larger but the maximum is smaller than the absolute value of the minimum. (For interpretation of the references to colour in this figure legend, the reader is referred to the web version of this article.)

with the depth: it is stronger (up to 2.7 $\times$ 10^{-3} m/s) and westward in a 25 km thick layer above the ocean bottom. Above this layer, the zonally averaged zonal flow is eastward but slower (at most 1.05 $\times$ 10^{-3} m/s), except at the surface in the southern hemisphere where it is westward at latitudes up to 50°S (see Fig. 9(b)). Taylor's columns are not captured, which might be due to the spatial resolution used. The zonally averaged radial velocity shows slow radial upwelling and downwelling. Downwelling mainly takes place at the high latitudes, except at the poles where upwelling occurs. The radial velocity can be much larger in the upper layers of the ocean, which is due to the spatial variations of the surface heat flux. The depth-averaged velocity flow does not exhibit global patterns but experiences strong local variations in both magnitude and orientation. The maximum depth-averaged speed is 1.14 $\times$ 10^{-4} m/s, which is two orders of magnitude smaller than the tidal depth-averaged flow speed. The surface flow is globally eastward and larger in the northern hemisphere (up to 1.13 $\times$ 10^{-4} m/s). In the southern hemisphere, the surface velocity is also eastward but it is smaller (the maximum is twice smaller than in the northern hemisphere). Near the bottom of the ocean, the flow is westward and larger in the southern hemisphere (up to 3.5 $\times$ 10^{-3} m/s). The ocean surface elevation is minimum (−0.0099 m) near the north pole and maximum near the south pole (at most 0.0065 m at (52.9° S, 64.7°E), although the elevation is negative at the south pole (see Fig. 10).

Taking into account both the tides and the thermally driven liquid motion (HFWT case) modifies the global aspect of the temperature field (with respect to HFNT). The tidal motion mixes the water, resulting in smaller temperature variations across the domain: the maximum is 0.115 K larger than the minimum. The surface temperature is maximum at the equator and decreases asymmetrically towards the poles: the local minimum is smaller at the north pole than at the south pole. The smaller temperature at the pole is consistent with the upwelling observed at this location in the purely thermally induced liquid motion. The elevation resulting from the thermally driven flow being constant, the surface elevation oscillates above a positive/negative elevation other modification of the elevation. The impact on the depth-averaged velocity field mainly consists in modifying its orientation. Indeed, although the thermally driven flow is slower, it's orientation does not change withe the time, which results in totally different spatial patterns (see Fig. 11). Although the main patterns consist of two gyres, the latter are located at much higher latitudes and their centre moves westward following a sinusoidal path centred on high latitude meridians (see Fig. 11). At perikron, the centres are located at (72.9°N, 115°E) and (62.3°S, 72.6°W). Depending on the position of the gyres, the flow is either south-eastward or north-eastward. For instance, on the 0° meridian, the flow is north-eastward when the southern gyre is located in the eastern hemisphere and south-eastward when the southern gyre is located in the western hemisphere (see Fig. 11). The 3D flow differs from the depth-averaged flow. The speed is maximum a few kilometres beneath the surface due to the surface friction. Depending on the location, the speed can increase with the depth as the maximum speed of the various layers are not located in the same area. Near the surface, the flow is globally eastward and two gyres are located near the poles while, near the bottom, the flow is globally westward

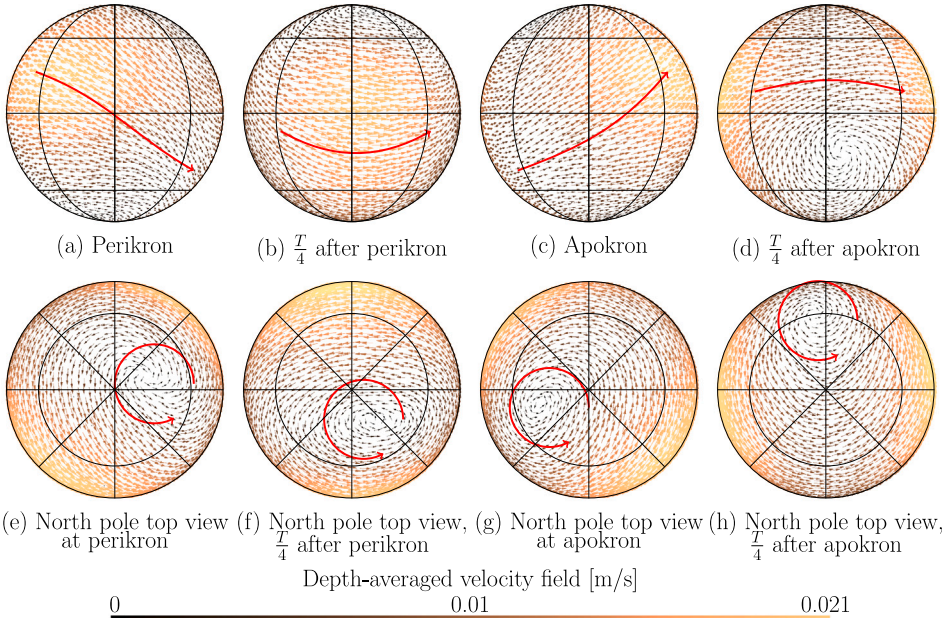

Fig. 11. Depth-averaged velocity field induced by the tidal forcing and the surface heat flux (HFWT case). For Panels (a), (b), (c), and (d) the north/south pole is at the top/bottom of the image, which is centred on the 0° meridian. Panels (e), (f), (g), and (h) correspond to an upper view of the north pole with the 0° meridian at the bottom of the image. The meridians/parallels are represented in black, with a 45° spacing. The depth-averaged velocity consists of two gyres whose centres are located near the poles and follow a sinusoidal path centred on the 60° meridians. The global flow orientation is illustrated by red arrows. While some aspects remain similar to the tidal flow (two gyres separated by a high speed zone), the flow orientation differs due to the new position of the gyres' centre. (For interpretation of the references to colour in this figure legend, the reader is referred to the web version of this article.)

with its orientation varying with time between north-westward and south-westward at both depths. The speed is larger in the northern hemisphere than in the southern one at the top and at the bottom of the ocean. The difference can reach up to 5 cm/s but is mostly about 1 cm/s and can be related to the thermally driven velocity field.

5. Sensitivity to parameter values

Several parameters are poorly constrained. In this section, a sensitivity analysis with respect to the depth of the water column, the friction coefficient, and the mechanical characteristics of the ice shell (by modifying A and B factors, see Eq. (3)) is conducted. We also study the thermally driven flow using a zonally uniform heat flux.

5.1. Influence of the free-surface ocean depth

Depending on the model used to study the internal structure of Titan, the depth of the ocean varies from less than 100 km to a few hundreds of kilometres (see Section 2). Therefore, the influence of the depth on the tidal motion is studied. This study is conducted on a free-surface ocean in order to decouple the impact of the ocean depth from that of the ice shell. The depths taken into account are 50, 75, 100, 150, 200, 250, 300, and 400 km. The lower and upper bounds correspond to the depth predicted by Baland et al. (2014), Mitri et al. (2014) and Lefevre et al. (2014), respectively.

Varying the ocean depth results in modification of both the elevation and depth-averaged velocity fields magnitude while the spatial patterns of these fields are not modified. The difference between the surface elevation of a 100 km deep ocean and the elevation of a deeper (FSO150, FSO200, FSO250, FSO300, FSO400) or shallower (FSO50, FSO75) ocean is shown in Fig. 12. The global patterns of this field are similar for each depth studied; although for 50 and 75 km deep oceans, the field is of opposite sign. Although the maximum surface elevation does not vary with the depth (see Table 1), the magnitude of this difference does increase with the depth (see Fig. 13). This can be explained by the fact that the ocean depth does not affect the range of the diurnal tidal component but rather impacts its phase. The larger the depth difference, the larger the phase variations and, hence, the larger the magnitude of the difference between the elevation fields. The phase lag increases with the depth (but not linearly) to reach about 2° for a 400 km deep ocean. For an ocean shallower than 100 km, the elevation variation is of opposite sign and is larger than for an ocean deeper than 100 km (see Fig. 13). Besides these variations, high frequency oscillations can also be observed in a 50 km deep ocean. Two tidal components stand out as their associated range are more than one order of magnitude larger than others (although 4 orders or magnitude smaller than the range associated to the diurnal component). The period and amplitude of these components are $\frac{1}{55}$ TD and $\frac{1}{56}$ TD and 4.04×10^{-3} m and 4.94×10^{-3} m, respectively. Both mean and maximum depth-averaged speeds decrease when the ocean depth is increased (see Table 1). However, the speed reduction is not large enough to compensate for the larger depth, resulting in an augmentation of the mean liquid transport[6] by 101 m^2/s between a 100 km and a 400 km deep ocean.

5.2. Influence of the friction

The influence of the friction on the tidal motion of a subsurface ocean is studied by varying the quadratic friction coefficient in SLIM2D. Therefore, it is not possible to isolate the effects of the upper surface friction from those of the bottom surface friction. Three uniform friction coefficients are taken into account: 2.5×10^{-3} (SSO25), 5×10^{-3} (SSO110), and 7.5×10^{-3} (SSO75).

Modifying the friction coefficient does not significantly impact the ocean surface elevation: the amphidromic points, the maximum elevation, and the spatial patterns are almost identical while the influence on the depth-averaged velocity field is small with respect to that of the other parameters (see Table 1). The larger the friction coefficient,

[6] The mean liquid transport is computed by multiplying the spatially averaged depth-averaged velocity by the (constant) ocean depth.

Table 1
Maximum ocean surface elevation (η_{max}), tidal range ($\Delta\eta$), mean depth-averaged current ($\|\boldsymbol{u}_m\|$), maximum depth-averaged current ($\|\boldsymbol{u}\|_{max}$), mean rate of energy dissipation by friction (P) for the various values of the parameters studied. H is the ocean depth, t is the relative thickness of the shell upper layer, δ is the ratio between the critical viscosity and the viscosity of the shell lower layer and C_D is the quadratic friction coefficient.

Name (parameter)	η_{max} [m]	$\Delta\eta$ [m]	$\|\boldsymbol{u}\|_m$ [cm/s]	$\|\boldsymbol{u}\|_{max}$ [cm/s]	$\log_{10}$P [W/m^2]
Free-surface oceans[a]					
FSO50 (H = 50 km)	8.9	17.8	1.87	2.43	−4.7
FSO75 (H = 75 km)	8.9	17.8	1.36	1.76	−5.12
FSO100 (H = 100 km)	8.89	17.8	1.04	1.35	−5.46
FSO150 (H = 150 km)	8.89	17.8	0.72	0.94	−5.94
FSO200 (H = 200 km)	8.89	17.8	0.55	0.72	−6.29
FSO250 (H = 250 km)	8.89	17.8	0.44	0.59	−6.57
FSO300 (H = 300 km)	8.89	17.8	0.37	0.49	−6.8
FSO400 (H = 400 km)	8.89	17.8	0.29	0.38	−7.15
Subsurface oceans[b]					
SSO110 (δ = 1, t = 10%)	8.44	16.9	0.97	1.27	−5.55
SSO140 (δ = 1, t = 40%)	8.44	16.9	0.97	1.27	−5.55
SSO0110 (δ = 0.1, t = 10%)	8.61	17.2	0.99	1.29	−5.53
SSO0140 (δ = 0.1, t = 40%)	8.55	17.1	0.98	1.28	−5.54
SSO1010 (δ = 10, t = 10%)	8.87	17.7	1.04	1.32	−5.50
SSO1040 (δ = 10, t = 40%)	8.7	17.4	1	1.3	−5.52
SSO25 ($C_D = 2.5 \times 10^{-3}$)	8.61	17.2	1.02	1.33	−5.49
SSO75 ($C_D = 7.5 \times 10^{-3}$)	8.61	17.2	0.99	1.28	−5.53
SSOG2 (γ_2 = 0.899[c])	7.74	15.5	0.926	1.2	−5.62
HFNT[d]	0.03	–	0.01	0.06	−8.64
HFWT[e]	9.06	17.9	0.95	2.01	−4.51

[a]The friction coefficient is $C_D = 2.5 \times 10^{-3}$.
[b]The friction coefficient is $C_D = 5 \times 10^{-3}$ and the ocean depth is H = 100 km.
[c]The deformation of Titan's core and mantle is taken into account by means of an attenuation factor, γ_2.
[d]These results are predicted by means of SLIM3D using a coarser mesh while ignoring the tidal forcing. The mean and maximum velocity are computed from the depth-averaged velocity field.
[e]These results are predicted by means of SLIM3D using a coarser mesh while taking into account the tidal forcing. The mean and maximum velocity are computed from the depth-averaged velocity field.

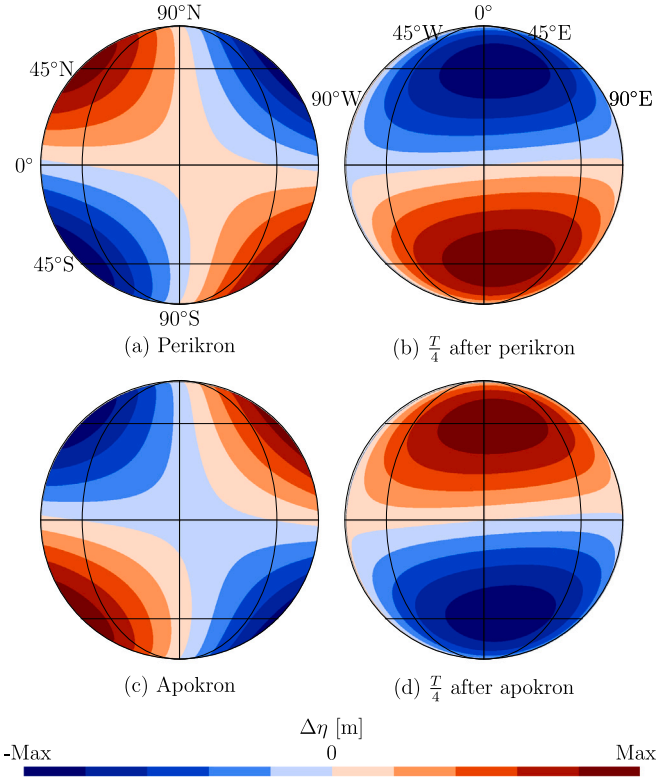

Fig. 12. Difference between the surface elevation of a 100 km deep ocean and a deeper (or shallower) ocean ($\Delta\eta$). The spatial patterns at (a) perikron, (b) 0.25 TD after perikron, (c) apokron and (d) 0.25 TD after apokron are similar while the amplitude (which is symmetric with respect to 0) varies with the depth. The maximum difference is 1.74×10^{-2} m, 2.67×10^{-2} m, 3.24×10^{-2} m, 3.62×10^{-2} m, and 4.53×10^{-2} m for 150, 200, 250, 300, and 400 km deep oceans, respectively. In the case of shallower ocean, the spatial patterns are identical but the difference is of opposite sign (the maximum being 4.7×10^{-1} m and 1.71×10^{-2} m for 50 and 75 km deep oceans, respectively). (For interpretation of the references to colour in this figure legend, the reader is referred to the web version of this article.)

the smaller the mean and maximum speeds. For instance, tripling the coefficient results in a maximum and mean speed 5×10^{-4} m/s and 4×10^{-4} m/s slower, respectively. The depth-averaged velocity orientation can locally vary with the friction.

While the friction cannot be disregarded, modifying the uniform friction coefficient does not significantly modify the tidal motion in the subsurface ocean.

5.3. Influence of the ice shell

The factors A and B quantifying the elastic and viscous deformations of the ice shell are function of the shell rheology and sub-layers relative thickness. These characteristics being poorly constrained, a sensitivity analysis with respect to A and B is conducted. Besides SSO110, eight configurations are studied: an elastic-like ($\delta = 0.1$, SSO0110 and SSO0140) and a fluid-like ($\delta = 10$, SSO1010 and SSO1040) lower layer making 90% and 60% of the shell thickness, a critical lower layer making 60% of the shell thickness (SSO140), a viscous deformation corresponding to SSO110 with the factor B being multiplied by 100 (which is large with respect to the expected values), an ice shell whose sole impact consists of the upper friction term, and an ice shell whose sole impact consists of the surface pressure term. These latter two configurations are studied to separate the effect of the surface pressure from that of the bottom friction. The elevation and depth-averaged velocity fields predicted are compared to SSO110 (see Section 4.2.2).

As its name suggests, an ice shell with an elastic-like lower layer results in a mostly elastic deformation of the ice shell as the viscous deformation tends towards zero as δ decreases. In our model, it results in increasing the surface pressure resulting from the horizontal gradient of the surface elevation. The impact of such an ice shell does not vary with the relative thickness of the lower layer. This behaviour was expected in the light of Figs. 3 and 14: for $\delta \leq 0.1$, A does not vary with the thickness while B, although experiencing minor variations, is almost zero. Under this configuration, the ocean experiences a smaller surface elevation, at most 8.44 m, which is 0.17 m smaller than for SSO110 (see Fig. 14(a)). The decrease results from the smaller range of the diurnal tidal component. Other aspects of the elevation field such as the location of the amphidromic points and the centre of the tidal bulges/troughs are similar to those predicted in SSO110. This ice shell also slows down the flow more significantly: the mean and maximum depth-averaged velocity are 2×10^{-4} m/s and 1.6×10^{-4} m/s slower than for SSO110 (see Fig. 14(b)).

A fluid-like lower layer also induces a mostly elastic deformation of the ice shell but reduces the surface pressure with respect to a viscoelastic/elastic-like lower layer. The thicker the lower layer, the smaller A and the larger B. The former is constant with respect to δ and its variation with respect to the upper layer thickness is much larger than that of B as the latter tends towards 0 as δ increases (see Figs. 3 and 14). The surface pressure being smaller than for SSO110, the maximum surface elevation and the depth-averaged speed are larger. The former increases by 0.23 m (resp. 0.09 m) for an upper layer making 10% (resp. 40%) of the shell thickness while the mean and maximum depth-averaged speed are larger by 2.3×10^{-4} m/s and 1.4×10^{-4} m/s (resp. 8.8×10^{-5} m/s and 7×10^{-5} m/s) (see Fig. 14).

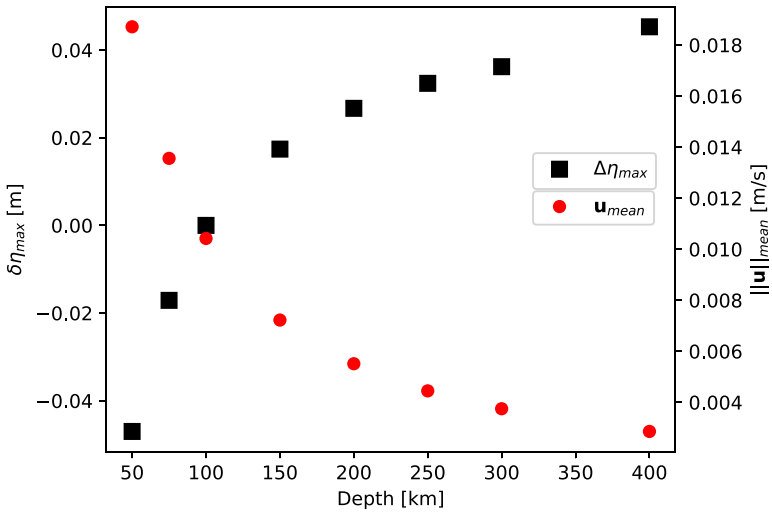

Fig. 13. Spatially and temporally averaged speed (circles) for various depths, and maximum variation between the associated surface elevation and the elevation of a 100 km deep ocean (squares). For the same depth variation, the elevation and speed variations are larger for an ocean shallower than 100 km than for a deeper ocean. The larger the depth difference, the larger the elevation and speed variations.

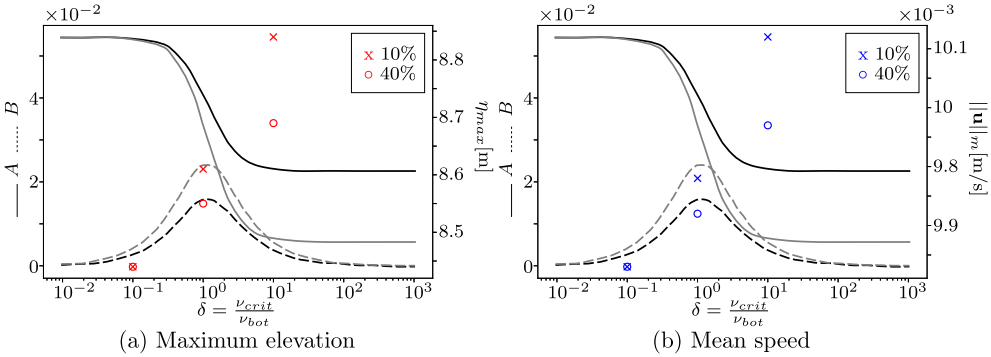

Fig. 14. (a) Maximum elevation and (b) mean depth-averaged speed for six of the configurations implemented: elastic-like ($\delta = 0.1$), critical ($\delta = 1$), and fluid-like ($\delta = 10$) lower layer with a upper layer making 10% (crosses) or 40% (circles) of the shell thickness. The dashed and full lines represent the value of B and A coefficients for a 10% thick upper layer (grey) and a 40% thick upper layer (black), respectively. The smaller the viscosity of the lower layer, the larger the elevation and depth-averaged speed. The thickness of the lower layer has no influence for an elastic-like layer and increases with the viscosity ratio: the thicker the lower layer, the larger the elevation and depth-averaged velocity.

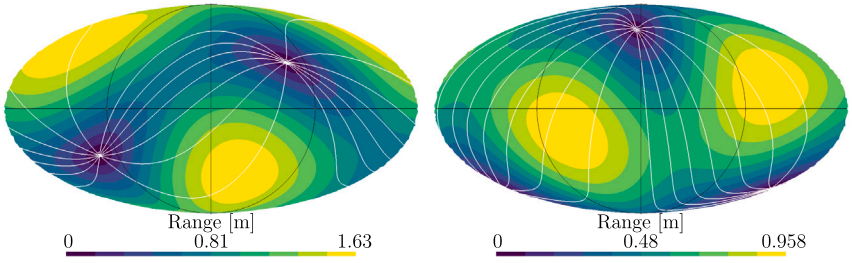

Fig. 15. Tidal range (in m) and phase (white lines, with a 22.5° spacing) of the tidal components whose associated range is the second (left panel, period of $\frac{1}{46}$ TD) and third (right panel, period of $\frac{1}{47}$ TD) largest (the largest being the diurnal) when the viscous part of the surface pressure is multiplied by 100. Both tidal components have two antipodal amphidromic points. They are displayed on a Mollweide projection of the sphere. They both have two amphidromic points, one in each atmosphere. (For interpretation of the references to colour in this figure legend, the reader is referred to the web version of this article.)

The other aspects of the depth-averaged velocity and elevation fields remain unchanged with respect to SSO110.

Slimming the viscoelastic lower layer results in an increase of the elastic aspect of the deformation while diminishing its viscous aspect (i.e. A increases and B decreases). Such modifications of the surface pressure induce a decrease of the surface elevation and depth-averaged speed. Their maximums decrease by 0.06 m (see Fig. 14) and 1×10^{-4} m/s, respectively. The other aspects of the elevation and depth-averaged velocity fields are not impacted.

We also study the case of a highly viscous shell by multiplying B by 100 in order to separate the effects of the viscous deformation from those of the elastic deformation. In this case, the range of the diurnal tidal component remains unchanged with respect to SSO110 but a phase lag of about $\pm 0.3°$ is observed. The latter is maximum near the amphidromic points and is positive/negative over almost a whole spherical octant. The main variation of the elevation field consists in the appearance of high frequency oscillations. They result in a maximum elevation larger by 0.75 m and occurring 0.15 TD after perikron. Several tidal components are associated to these oscillations. Those that

have the largest range (1.63 m and 0.958 m) have a period of $\frac{1}{46}$ and $\frac{1}{47}$ TD (see Fig. 15). The depth-averaged velocity field also undergoes variations: although it consists of two gyres separated by a ring of high velocity flow, the gyres centres do not follow a sinusoidal motion but rather a helicoidal one around the equator. This back-and-forth motion of the centre is related to the small period oscillations of the elevation. It also results in centres located at higher latitudes than in SSO110 (up to 12°). The magnitude of the depth-averaged velocity field is also impacted. The mean speed is less impacted than the maximum speed: the former is larger by 9×10^{-5} m/s) while the latter is larger (by 2.7×10^{-3} m/s). We conclude that the viscous deformation does not impact the global behaviour of the diurnal motion but can generate high frequency oscillations impacting both the depth-averaged velocity and elevation fields.

An ice shell deforming as the ocean (i.e. the surface pressure term is zero) does not modify the surface elevation in terms of amplitude or spatial patterns. The depth-averaged velocity field is similar to that of a free-surface ocean (FSO100) although the maximum and mean speed are slightly smaller, by 3×10^{-4} m/s and 3×10^{-4} m/s, respectively. In the opposite case of a friction-less ice shell, the surface elevation is similar to that of a subsurface ocean (SSO110), with a maximum elevation 0.28 m smaller than the maximum predicted for a free-surface ocean (FSO100). The depth-averaged velocity field is similar to that of a subsurface ocean (SSO110) but the maximum and mean speed are slightly larger, by 4×10^{-4} m/s and 4×10^{-4} m/s, respectively. We conclude that the surface pressure impacts the depth-averaged velocity field more significantly than the friction and, unlike the latter, also impacts the surface elevation.

5.4. Influence of the surface heat flux

We conducted a 3D simulation using a zonally uniform heat which is maximum (7.5×10^{-3} W/m^2) at the poles and decreases towards the equator where it is 5.6×10^{-3} W/m^2. Such a boundary condition also results in a mixed ocean with a temperature larger at the surface than at the bottom by 0.3 K. Zonal and meridional variations also take place but they are one order of magnitude smaller. For instance, the surface temperature is maximum at the equator and decreases towards the poles but the variations are about 0.02 K. The ocean surface elevation is negative at the poles, with a minimum of −0.06 m at the south pole and maximum at the equator (0.01 m). The zonally averaged temperature profile is similar to that predicted in HFNT, which makes sense as the zonal average of the heat flux used in HFNT is similar to the zonal heat but with a small asymmetry between the northern and southern hemispheres. The zonally averaged zonal velocity is different: it is westwards at the surface and bottom of the ocean and eastward elsewhere. The zonally averaged radial velocity consists in downwelling in an area extending from the poles to the 80° meridian and upwelling in the upper layers elsewhere. The depth-averaged velocity field is the extension of a westward gyres centred at the north pole and an eastward gyre centred at the south pole. The depth averaged speed is much stronger in the northern hemisphere than in the southern one, resulting in a change of direction taking place near the 45° meridian.

Taking into account both the tidal forcing and the zonally uniform surface heat flux results in velocity fields (both 3D and depth averaged) similar to those of HFWT although the speed is slightly smaller. For instance, the maximum is smaller by 0.005 m/s (6.5% of its value). The temperature and elevation fields are also similar to those of HFWT, although the variations of the temperature are slightly smaller than in HFWT: there is 0.104 K between the minimum and maximum temperature.

6. Discussion

6.1. Energy dissipation rate by friction

The amount of energy dissipated within a subsurface ocean is a sticking point due to the poorly constrained processes at stake. Two approaches were developed: Tyler (2008, 2009, 2011, 2014, 2020) studied the energy dissipated in a subsurface ocean as a function of its depth and the dissipation timescale while avoiding prescription of the specific dissipation process, whereas Chen et al. (2014), Beuthe (2016), Hay and Matsuyama (2017, 2019), Matsuyama (2014) and Matsuyama et al. (2018) studied the energy dissipated assuming specific processes such as friction or interactions with the ice shell. In this article, we focus on the liquid motion within the ocean. Using the elevation and depth-averaged velocity field predicted, we were able to compute the rate of kinetic energy dissipated by friction and the power developed by the surface pressure force at the top of the ocean. The spatially and temporally averaged rate of energy dissipated by friction over a tidal period (in W/m^2) is computed following the same approach as, e.g., Hay and Matsuyama (2017) and Sears (1995): $\dot{E} = \frac{1}{T}\int_0^T \frac{-1}{\Gamma}\int_\Gamma \rho c_D u^3 \mathrm{d}\Gamma \mathrm{d}t$ where Γ is the whole top and bottom surfaces of the domain, T is the diurnal period, ρ is the liquid mean density, u is the depth-averaged speed, and c_D is the quadratic bottom friction coefficient. The spatially and temporally averaged power developed by the surface pressure force (in W/m^2) reads (Deleersnijder and Vincent, 2020)

$$P = \frac{1}{T}\int_0^T \frac{1}{\Gamma}\int_\Gamma -p(z=\eta)\frac{\partial \eta}{\partial t}\mathrm{d}\Gamma \mathrm{d}t = \frac{1}{T}\int_0^T \frac{-1}{\Gamma}\frac{d}{dt}\int_\Gamma \frac{\rho g A}{2}\eta^2 \mathrm{d}\Gamma - \frac{\rho g B}{\Gamma}\int_\Gamma \left(\frac{\partial \eta}{\partial t}\right)^2 \mathrm{d}\Gamma \mathrm{d}t \quad (8)$$

For FSO100 and SSO110, the energy dissipated by friction is $\mathcal{O}(10^{-6})$ W/m^2, which is too small to explain by itself the heat flux computed by Kvorka et al. (2018). The contribution of the eccentricity and obliquity tidal forces to the kinetic energy dissipation rate is five orders of magnitude larger for the obliquity tidal force ($\mathcal{O}(10^{-6})$ W/m^2) than for the eccentricity tidal force. The mechanical characteristics of the ice shell lying above the ocean have a small effect on the energy dissipated by friction within the ocean: the dissipation rate varies by less than 13%. The energy dissipation rate would nevertheless increase significantly if the ice shell pushes the ocean towards critical damping (i.e. to the left in Figs. 4 and 5) by means of a mechanism not taken into account. The influence of the ocean depth is much larger with a dissipation rate 48 times larger for a 100 km deep ocean than for a 400 km deep ocean. The larger the depth (friction coefficient), the smaller the energy dissipated. This behaviour is in accordance with the solution domain computed (see Fig. 4) and was also predicted by Chen et al. (2014) and Hay and Matsuyama (2017, 2019).

The shell influences the phase speed of waves such as the Poincaré waves and equatorial Rossby and Kelvin waves: the latter increases with A and decreases with B. However, the variations are not large enough for these waves to be resonantly forced in the case of the ocean configurations studied by means of SLIM. While resonant states are not reached, this conclusion cannot be extended to other ocean configurations (i.e. other ocean depths and/or friction coefficients). Indeed, as seen in the solution domains figures in Tyler (2011, 2014, 2020), and in Figs. 4, 5 of this paper, high-power (resonantly forced) tidal states are possible for thick ocean depths (or equivalent depths[7]) on synchronously rotating satellites in at least two cases: where there is significant obliquity, or where there is large damping (i.e. damping time scale similar to that of the forcing). Internal waves could also result in a large amount of energy dissipation. Such waves were not

[7] The equivalent depth is the "depth" that would be required for the wave speed of barotropic tides to match the internal wave speed (which depends on stratification).

observed for the 100 km deep subsurface ocean with a uniform bottom heat flux studied.

The power associated with the forces exerted by the ocean on the ice shell is much larger than the rate of energy dissipated by friction, it is $\mathcal{O}(10^{-3})$ W/m^2, which is in line with the solution domain (see Fig. 5). This power is two orders of magnitude smaller for the obliquity tide ($\mathcal{O}(10^{-5})$ W/m^2) than for the eccentricity tide. The main contribution to the energy loss from the ocean point of view is thus the transfer of potential energy from the ocean to the ice shell, which is three orders of magnitude larger than the energy dissipated within the ocean by friction. The obliquity driven tidal motion is the main contribution to the energy dissipation by friction in the ocean while the eccentricity driven tidal motion leads to a transfer of the potential energy to the shell (where it could be dissipated by various phenomena) but results in a small amount of energy dissipation in the ocean itself. The impact of the ocean depth on the power developed by the surface pressure force is not studied but is expected to be null as the pressure is a function of the ocean elevation and the magnitude of the latter does not vary with the depth.

6.2. Influence of the parameters

Several aspects of Titan's subsurface ocean are poorly constrained. Some of them, such as the mean liquid density, are not considered here, as their influence on barotropic phenomena is negligible, while others are interconnected, which makes it difficult to distinguish their impact from that of other parameters. Therefore, the influence of three major parameters is discussed while the others are disregarded. These parameters are the ocean depth, the mechanical characteristic of the ice shell lying at the top of the ocean, and the heat flux used as surface boundary condition. The parametric studies are limited by the actual knowledge of the ocean. For instance, the depth is assumed to be constant although the top and bottom could be undulated due to spatial variations of the heat fluxes. Such limitations are unfortunately unavoidable as there is a large number of realistic configurations.

6.2.1. Influence of the ocean depth

Modifying the ocean's depth mainly results in a phase lag of the surface elevation and modifications of the depth-averaged speed. The former and the latter respectively increases and decreases when the depth is increased. The phase lag could be explained by the influence of the ocean depth on the phase speed of the gravity waves in shallow water. The latter is proportional to the square root of the depth. Modifying the depth therefore results in variation of the phase speed, which could explain the phase lag observed in the elevation field. In the case of a 50 km deep free surface ocean, high frequency oscillations, which do not appear for larger depths, were predicted. One explanation could be that the high frequency oscillations occurring in deeper oceans are not captured by our model due to the time step. This assumption was tested by conducting a simulation with an export time step divided by 5 (i.e. 10^{-3} TD) for a 100 km deep ocean.[8] No high frequency oscillation being observed, this explanation is ruled out. Another explanation could be that a normal mode of the ocean is excited in the case of small ocean depths. Indeed, the shallower the ocean, the longer the natural period. The small period oscillations in a 50 km deep ocean could be due to a normal mode which would not be excited in deeper ocean due to its smaller natural period.

In this study, we assumed a uniform bathymetry due to the absence of data regarding the space variation of the water column depth. Nevertheless, there likely are spatial variations of the depth due to the local melting/freezing at the upper and bottom boundaries. Such crests/troughs could locally speed up/slow down the flow and modify its orientation. For instance, freezing taking place at the same longitude and latitude both at the upper and bottom surface could results in a local variations of the depth-averaged velocity orientation and magnitude and ocean surface elevation.

6.2.2. Influence of the ice shell rheology

The tidal scenario is similar to the Europa tidal scenario for the values of A and B corresponding to an elastic-like, fluid-like, or viscoelastic configuration. The tidal response could therefore be described, as a first approximation, by the analytical solution of Tyler (2008). The effect of the ice shell is similar for the elastic-like, fluid-like, and viscoelastic configurations studied: it decreases the amplitude of the surface elevation and it slows down the flow while the global patterns of the elevation and depth-averaged velocity fields remain similar. Such differences make sense as the effects of the shell are modelled by modifying the surface pressure term and doubling the friction coefficient. The elastic deformation of the ice shell increases the horizontal pressure gradient (which exists in the "standard" shallow water equations, its effect is thus similar to increasing the mean gravitational acceleration) while the viscous deformation results in a smaller, 90° out-of-phase, surface pressure. Depending on the rheology and thickness of the lower layer, the decrease in elevation and in depth-averaged velocity (see Fig. 14) varies: the larger A, the smaller the elevation and speed. The factor B has the same effect within the range corresponding to Fig. 14. In order to highlight the effect of the viscous deformation, we conducted a simulation where B is multiplied by 100 (which is large with respect to the expected values). In this case, the tidal scenario differs: the flow is speeded up, the elevation is larger and the spatial patterns of these fields are different from those predicted in SSO110. These modifications are mainly due to the high frequency oscillations resulting from the viscous surface pressure that is out of phase with respect to the elevation field.

In our study of the impact of the ice shell deformation, the shell is assumed to be made of two layers: an elastic upper layer and a lower layer which can be elastic-like, viscoelastic, or fluid-like, depending on its the ratio between the critical viscosity and its viscosity (see Section 3.2). Using a different rheology could slightly modify the results presented but this is taken into account by studying the impact of the shell deformation for different configurations, which likely spans the rheology variations resulting from the use of another model.

Our approach does not take into account the feedback of the ocean on the ice shell deformation. This could be circumvented by coupling an ocean model and a deformation model. While the impact of the ice shell on the tidal motion should not be disregarded, the variations associated with the different shell mechanical characteristics implemented are small, except for a highly viscous shell. Therefore, we do not think a more elaborate approach is necessary as we consider our model to be well suited for a first approach when studying the tidal motion within the subsurface ocean — it allows evaluating the significance of the impact of the ice shell deformation on the liquid motion. However, we recognise that a more complex model should be developed to improve the accuracy. While the impact of improving the representation of the shell deformation on the tidal motion is expected to be small, it could be interesting as part of a more elaborate study. Indeed, we assume a uniform bathymetry and a smooth ice–water interface. These hypotheses are made because of the lack of information although spatial variations of these parameters are expected to have a significant impact on the tidal motion. For instance, spatial variations of the ice shell properties and/or methane clathrates could results in local variations of A and B. Their impact on the tidal motion would be a function of their spatial derivative: the steeper the gradient, the larger the impact. In order to study such phenomena, a much more elaborate model should be built and data unavailable to this day are needed. Such a model should also take into account the surface heat fluxes and the crystallisation/melting processes at the top and bottom of the ocean. The latter impact the

[8] This ratio of 5 was selected because the wave velocity is a function of the square root of the depth and is hence modified by a factor $\sqrt{2}$ in a 100 km deep ocean with respect to the 50 km deep ocean.

deformation of the shell in a way that only a complex 3D model could capture. In order to model the impact of these phenomena on the ocean, a time-varying bathymetry should be implemented and the latent heat flux should be taken into account. Building such a model is beyond the scope of this article.

6.2.3. Influence of the surface heat flux

We tested two scenarii: the surface heat flux derived by Kvorka et al. (2018) and a zonally uniform heat flux that corresponds to the heat flux of Kvorka et al. (2018) when only the degrees 2, 4 and 6 and order 0 are taken into account). Some aspects of the results are hence expected to be similar while the differences are due to the zonal variations of the heat flux. In both case, the temperature field tends to decrease with the depth (about 0.3 K between the surface and the bottom). The zonal and meridional variations are even smaller. In both case, the elevation is $\mathcal{O}(10^{-2})$ m but the spatial patterns are different: the area where the surface elevation is positive is larger with the zonal heat flux but is located further away from the poles and the maximum elevation is smaller (0.01 m instead of 0.065). The velocity differs significantly depending on the heat flux. For instance, in the case of Kvorka et al. (2018)'s heat flux, the speed is larger in the northern hemisphere than in the southern while this is not the case with the zonally uniform heat flux, although the velocity field is not symmetric with respect to the equator. The zonally averaged zonal velocity have a vertical structure similar in both cases but the velocity orientation is in the opposite direction (i.e. eastward at the bottom and at the surface) with the zonal heat flux.

On the other hand, the results are almost identical when comparing the liquid motion induced by both the tides and the surface heat fluxes: the global patterns are the same but the speed/temperature can change by a few percents. In both cases, the tidal forcing is the main driver behind the liquid motion, although the latter differs significantly from the tidal motion. The zonal variations of the surface heat flux, while impacting the thermally driven liquid motion, seem not to have an impact large enough to be visible when taking into account the tidal forcing. This could be due to the fact that the liquid is driven away by the tidal motion before being significantly heated/cooled. It results in much smaller temperature variations over the ocean.

The surface heat flux impacts all the aspects of the liquid motion. We deemed a good representation of the heat flux necessary to be confident with the thermally driven liquid motion as the latter changes significantly depending on the spatial distribution of the heat flux. Nevertheless, we do not aim at studying the thermally driven liquid motion on its own but rather at studying its interaction with the tidal motion. In this regards, the zonal variations of the surface heat flux could be disregarded as their impacts on the liquid motion is hardly visible in our results.

6.3. Deformation of the bottom of the ocean

Similarly to the ice shell at the top of the ocean, the bottom of the ocean deforms due to the tidal forcing, resulting in an attenuation of the forcing acting on the ocean. This effect can be modelled by means of an attenuation factor (similarly to what is done for the surface lakes and seas). The real parts of the Love numbers k_2 and h_2 are 0.12 and 0.221 (Hay and Matsuyama, 2017), resulting in an attenuation factor $\gamma_2 = 0.899$, which is close to unity. In an enclosed domain without internal separation, multiplying the forcing by the attenuation factor results in decreasing the surface elevation and depth-averaged speed without modifying the spatial patterns. A numerical simulation is conducted for a subsurface ocean whose bottom deformation results in an attenuation of the forcing. The predicted elevation decreases, leading to a maximum elevation of 7.74 m (which is the value obtained by multiplying the maximum elevation predicted for SSO110 by γ_2). The mean and maximum depth-averaged speed are also smaller, by 6×10^{-4} m/s and 9×10^{-4} m/s, respectively. The energy dissipated by friction within the ocean is therefore smaller. Other aspects of the elevation and depth-averaged velocity fields are not modified by the attenuation factor. The elevation and depth-averaged speed predicted by our model should therefore be regarded as an upper bound.

6.4. Thermally driven flow

The temperature gradient resulting from the heat fluxes at the top and bottom of the ocean can generate a thermally driven flow. The latter interacts with the tidal flow, modifying the flow orientation and locally increasing the speed and, hence, the heat production through viscous dissipation.

In this article, we assume a uniform bottom heat flux while the latter is expected to vary spatially. Indeed, according to Choblet et al. (2017), the heat transfer through the high pressure ice layer mainly consists of water transport in hot convective plume conduits. This conduits would result in local increase of the heat flux. In the absence of tidal motion, such a bottom boundary condition induces narrow cylindrical chimneys which broaden over time until they become baroclinically unstable (Goodman and Lenferink, 2012). On Europa, the currents associated with these plumes can reach 5 cm/s (Goodman and Lenferink, 2012). The tidal motion would likely prevent the formation of purely vertical chimneys due to the horizontal transport associated with the tides[9] while the chimneys could locally modify the flow orientation and magnitude. Depending on the size of the hot convective plume conduit (and the resulting chimneys), the bottom heat flux could impact the lower ocean layers, locally modifying the liquid motion, or the whole ocean. The vertical transport of hot water from these plumes to the upper ice shell could partially explain the variations of the surface heat flux. In order to study their impacts on the tidal motion, the spatial distribution as well as the characteristics of the water in the plume should be known.

Other phenomena which could modify the temperature-driven flow are also neglected. The heat production by dissipation within the ocean as well as the latent heat flux are not taken into account in the ocean heat balance. Indeed, the melting/freezing processes could play a significant role by modifying locally the heat flux and bathymetry. Besides heating/cooling the water, the melting and freezing processes would also impact the density by decreasing/increasing the salinity (see Section 6.5 for a discussion about the salinity). These phenomena should be taken into account in the model in order to increase the accuracy. Nevertheless, this is not the goal of the present study which aims at evaluating the thermally driven flow with regards to the tidal one. Although their impacts on the liquid motion can differ by order(s) of magnitude, they both impact the liquid motion in a way that cannot be disregarded. Therefore, a more complex model should be build to construct a more realistic representation of the thermal aspect of our study but this is beyond the scope of this article.

6.5. Salinity

The salinity was shown to results in global circulation in Europa's (Ashkenazy and Tziperman, 2021) and Enceladus' ocean (Kang et al., 2022; Zeng and Jansen, 2021). Kang et al. (2022) and Zeng and Jansen (2021) showed that, at modest pressure, the thermal expansion coefficient is negative for low enough temperature and salinity (< 20 psu), resulting in a density increasing with the temperature. Such anomalous expansion results in a stratified layer in Enceladus' upper ocean (Zeng and Jansen, 2021). This situation will not develop on Titan as the pressure under Titan's ice shell is too high for this anomalous expansion to take place (Kang et al., 2022) and the mean salinity is

[9] This assumption is not based on numerical results but on the observation of wind induced updraft rupture below cumulus: the horizontal wind velocity can tear apart the updraft, which results in isolated updraft bubbles.

expected to be larger than 20 psu to meet the mean ocean density predicted by, among others, Baland et al. (2014) and Mitri et al. (2014). The only impact of the salinity on the global circulation is thus through the density, by a mechanism similar to the one taking place in terrestrial oceans. Variation of salinity in the domain is expected to be induced by melting/freezing at the surface of the ocean and fresh water income at the bottom of the ocean. The impact of salinity and temperature on the density can be similar or differ depending on the location and the phenomena at stakes. The income of fresh water at the bottom of the ocean will increase the buoyancy similarly to the heating of the water. The buoyancy effects at the bottom of the ocean are hence well represented in our model although they are underestimated due to the fact that the impact of the salinity field is not taken into account. On the other hand, melting events at the surface of the ocean also result in fresh water income but the latent heat flux cools down the water, resulting in opposite effects on the buoyancy. The effect of the salinity at the surface of the ocean is thus much more tricky: depending on the main contributor to the density variations (temperature or salinity), the results could differ. Our results should be close to a temperature-driven scenario although the temperature effects might be overestimated as salinity dwarf them. A salinity-driven scenario such as the one predicted in Europa's ocean by Ashkenazy and Tziperman (2021) could change the physics at the surface of the ocean. Indeed, a freshwater layer at the top of ocean due to ice melting could function as a blanket that partially insulates the deep ocean from the ice and may create a stronger vertical temperature gradient than an ocean without the layer (Zhu et al., 2017). Properly dealing with the salinity field is a complex task which is beyond the scope of this article and would require to couple SLIM with an ice model to take into account the effects of melting and freezing.

6.6. Comparison with convection models

The thermally driven liquid motion in Titan global ocean was studied by means of convection models. Although the spatial and time scales can differ, it can be interesting to compare our results to the scenarii predicted by means of these models. Amit et al. (2019) studied the cooling patterns in Titan's global subsurface ocean without taking into account the tidal motion. They concluded that, based on the heat flux models of Kvorka et al. (2018), the polar cooling scenario prevails at the top of Titan's ocean. The surface temperature predicted by SLIM is consistent with this conclusion as the temperature is higher at the equator and lower near the poles. Unlike (Amit et al., 2019), we observed an asymmetry between the northern and southern hemisphere. The temperature differences are small (at most 0.15 K), although larger than that predicted by Amit et al. (2019) (1.4×10^{-3} for an average heat flux of 8 mW/m^2). Soderlund (2019) also studied the ocean currents induced by the convection in subsurface oceans. The convection models that were predicted for Titan are not consistent with the heat flux derived by Kvorka et al. (2018) from the topography. The topography could be explained either by a less dense marine ice at the equator or by another convection model (Fig. 3e in Soderlund, 2019) for which rotational effects are sufficient to maximise heat flow and melting at the pole, which would require a stably stratified salinity gradient (Soderlund, 2019). While some aspects of the flow induced by the heat flux are similar to the latter convection model (small radial velocity, larger heat flux at the poles), others are not. This could be explained by the fact that (1) salinity is not taken into account in our model so we are unable to model the impact of an hypothetical stratification, (2) we implemented a no slip condition at the top and bottom boundary while Soderlund (2019) implemented free slip conditions (this is discussed in her article).

7. Conclusion

The existence of an ocean lying beneath Titan's icy surface is ascertained by several observations and measurements. This ocean has a substantial impact on the deformation of Titan as well as the energy dissipated. Various studies focus on these aspects (e.g., Tyler, 2008, 2020; Matsuyama et al., 2018; Hay and Matsuyama, 2019). We studied the liquid motion within the global subsurface ocean using an Earth-based model, SLIM, which can solve the equations on a sphere and was adapted to the specific conditions of Titan. The 2D and 3D versions were used to predict the tides and the thermally driven flow, respectively. The mechanical characteristics of the ice shell and the depth of the ocean being poorly constrained at present, a sensitivity analysis with respect to these parameters was conducted.

Our model predicts a tidal scenario similar to the Europa tidal scenario described by Tyler (2008). The elevation field is made of two troughs/bulges rotating around Titan and resulting in a diurnal tide whose maximum amplitude is 8.9 m. The associated depth-averaged velocity field consists of two gyres separated by an area of high speed flow. The centres of the gyres move westward following a sinusoidal path centred on the equator and whose amplitude is small. Taking the ice shell lying above the ocean into account results in a smaller surface elevation and a slower tidal flow but does not modify the spatial patterns of these fields. The magnitude of the depth-averaged speed and elevation reduction depends on the mechanical characteristics of the ice shell. For instance, the impact of a fluid-like ice shell is smaller than that of a viscoelastic or elastic shell. The tidal scenario is similar to the Europa tidal scenario for each of these configurations, suggesting (Tyler, 2008)'s simple analytical solution to the tidal response may be a good first description of the tidal response on many bodies with thick oceans under ice and significant obliquity (e.g. an obliquity angle (in radians) comparable to or larger than the eccentricity). The other poorly constrained parameter whose influence is studied is the ocean depth. Modifying the latter results in a phase lag in the elevation field and a slowing down of the flow velocity by a few mm/s (which is $\mathcal{O}(10)\%$). These results suggest that, while the influence of the ice shell on the liquid motion cannot be disregarded, the latter is less sensitive to the mechanical characteristics of the shell. Therefore, while it is important to have a good estimation of the ocean depth and to take into account the shell, discrepancies about its mechanical characteristic can be allowed in modelling the tidal motion.

The ocean experiences heating/cooling at its top and bottom. These heat fluxes result in a constant surface elevation which is three orders of magnitude smaller than the tidal elevation. The resulting flow differs from the tidally induced one: the gyres are located at higher latitudes and they rotate around the poles following a sinusoid centred on the 60° parallel. These results suggest that, while a 2D model is efficient to model the tides of the subsurface ocean and study the influence of the depth and shell deformation, a 3D model is needed to study the liquid motion as the impact of the thermally driven flow cannot be disregarded regarding the global orientation of the flow and the local variation of the speed. While the surface heat flux should be taken into account, its zonal variations could be disregarded as they do not impact the liquid motion significantly due to the tidal motion moving the water away before it is cooled/heated significantly enough to results in density variations impacting the liquid motion.

Acknowledgements

Computational resources have been provided by the high performance computing group of the Université catholique de Louvain (CISM/UCL) and the Consortium des Équipements de Calcul Intensif en Fédération Wallonie Bruxelles (CÉCI) funded by the Fond de la Recherche Scientifique de Belgique (F.R.S.-FNRS) under convention 2.5020.11 and by the Walloon Region. Eric Deleersnijder is an honorary Research associate with the F.R.S.-FNRS. This research is partially

funded by the Belgian PRODEX, managed by the ESA, in collaboration with the Belgian Federal Science Policy Office. Véronique Dehant has received funding from the European Research Council (ERC) under the European Union's Horizon 2020 research and innovation programme (Advanced Grant agreement No 670874 RotaNut — Rotation and Nutation of a wobbly Earth and Synergy Grant agreement No 855677 GRACEFUL — GRavimetry mAgnetism and CorE FLow). Robert Tyler acknowledges support from the NASA Cassini Data Analysis Program.

References

Amit, H., Choblet, G., Tobie, G., Terra-Nova, F., Čadek, O., Bouffard, M., 2019. Cooling patterns in rotating thin spherical shells–application to Titan's subsurface ocean. Icarus 113509. http://dx.doi.org/10.1016/j.icarus.2019.113509.

Ashkenazy, Y., Tziperman, E., 2021. Dynamic Europa ocean shows transient Taylor columns and convection driven by ice melting and salinity. Nature Commun. 12 (1), 1–12. http://dx.doi.org/10.1038/s41467-021-26710-0.

Baland, R.-M., Tobie, G., Lefèvre, A., Van Hoolst, T., 2014. Titan's internal structure inferred from its gravity field, shape, and rotation state. Icarus 237, 29–41. http://dx.doi.org/10.1016/j.icarus.2014.04.007.

Baland, R.-M., Van Hoolst, T., Yseboodt, M., Karatekin, O., 2011. Titan's obliquity as evidence of a subsurface ocean? Astron. Astrophys. 530, A141. http://dx.doi.org/10.1051/0004-6361/201116578.

Barr, A.C., Citron, R.I., Canup, R.M., 2010. Origin of a partially differentiated Titan. Icarus 209 (2), 858–862. http://dx.doi.org/10.1016/j.icarus.2010.05.028.

Béghin, C., Sotin, C., Hamelin, M., 2010. Titan's native ocean revealed beneath some 45 km of ice by a schumann-like resonance. C. R. Geosci. 342 (6), 425–433. http://dx.doi.org/10.1016/j.crte.2010.03.003.

Beuthe, M., 2015a. Tidal Love numbers of membrane worlds: Europa, Titan, and co. Icarus 57 (258), 239–266. http://dx.doi.org/10.1007/s10236-006-0093-y.

Beuthe, M., 2015b. Tides on Europa: The membrane paradigm. Icarus 248, 109–134. http://dx.doi.org/10.1016/j.icarus.2014.10.027.

Beuthe, M., 2016. Crustal control of dissipative ocean tides in Enceladus and other icy moons. Icarus 280, 278–299. http://dx.doi.org/10.1016/j.icarus.2016.08.009.

Castillo-Rogez, J.C., Lunine, J.I., 2010. Evolution of Titan's rocky core constrained by Cassini observations. Geophys. Res. Lett. 37 (20), http://dx.doi.org/10.1029/2010GL044398.

Chen, E., Glatzmaier, G., Nimmo, F., 2010. Modeling the dynamics of icy satellite subsurface oceans with focus on implications for spacecraft observables. In: Lunar and Planetary Science Conference. 41, p. 1454.

Chen, E., Nimmo, F., Glatzmaier, G., 2014. Tidal heating in icy satellite oceans. Icarus 229, 11–30. http://dx.doi.org/10.1016/j.icarus.2013.10.024.

Choblet, G., Tobie, G., Sotin, C., Kalousova, K., Grasset, O., 2017. Heat transport in the high-pressure ice mantle of large icy moons. Icarus 285, 252–262. http://dx.doi.org/10.1016/j.icarus.2016.12.002.

Comblen, R., Legrand, S., Deleersnijder, E., Legat, V., 2009. A finite element method for solving the shallow water equations on the sphere. Ocean Model. 28 (1–3), 12–23. http://dx.doi.org/10.1016/j.ocemod.2008.05.004.

Consolmagno, G.J., Lewis, J.S., 1978. The evolution of icy satellite interiors and surfaces. Icarus 34 (2), 280–293. http://dx.doi.org/10.1016/0019-1035(78)90168-9.

Cushman-Roisin, B., Beckers, J.-M., 2011. Introduction To Geophysical Fluid Dynamics: Physical and Numerical Aspects. Academic Press.

Deleersnijder, E., Vincent, D., 2020. On the mechanical energy budget of Titan's subsurface ocean: a simple fluid-structure interaction problem. Technical Report, UCLouvain, URL: http://hdl.handle.net/2078.1/231552.

Dunaeva, A., Kronrod, V., Kuskov, O., 2016. Physico-chemical models of the internal structure of partially differentiated Titan. Geochem. Int. +54 (1), 27–47. http://dx.doi.org/10.1134/S0016702916010043.

Fortes, A.D., 2012. Titan's internal structure and the evolutionary consequences. Planet Sp. Sci. 60 (1), 10–17. http://dx.doi.org/10.1016/j.pss.2011.04.010.

Fortes, A.D., Grindrod, P.M., Trickett, S., Vočadlo, L., 2007. Ammonium sulfate on Titan: Possible origin and role in cryovolcanism. Icarus 188 (1), 139–153. http://dx.doi.org/10.1016/j.icarus.2006.11.002.

Geuzaine, C., Remacle, J.-F., 2009. Gmsh: A 3-D finite element mesh generator with built-in pre-and post-processing facilities. Int. J. Numer. Methods Eng. 79 (11), 1309–1331. http://dx.doi.org/10.1002/nme.2579.

Goodman, J.C., Lenferink, E., 2012. Numerical simulations of marine hydrothermal plumes for Europa and other icy worlds. Icarus 221 (2), 970–983. http://dx.doi.org/10.1016/j.icarus.2012.08.027.

Hay, H.C., Matsuyama, I., 2017. Numerically modelling tidal dissipation with bottom drag in the oceans of Titan and Enceladus. Icarus 281, 342–356. http://dx.doi.org/10.1016/j.icarus.2016.09.022.

Hay, H.C., Matsuyama, I., 2019. Nonlinear tidal dissipation in the subsurface oceans of Enceladus and other icy satellites. Icarus 319, 68–85. http://dx.doi.org/10.1016/j.icarus.2018.09.019.

Iess, L., Jacobson, R.A., Ducci, M., Stevenson, D.J., Lunine, J.I., Armstrong, J.W., Asmar, S.W., Racioppa, P., Rappaport, N.J., Tortora, P., 2012. The tides of Titan. Science 337 (6093), 457–459. http://dx.doi.org/10.1126/science.1219631.

Jackett, D.R., McDougall, T.J., Feistel, R., Wright, D.G., Griffies, S.M., 2006. Algorithms for density, potential temperature, conservative temperature, and the freezing temperature of seawater. J. Atmos. Ocean. Technol. 23 (12), 1709–1728. http://dx.doi.org/10.1175/JTECH1946.1.

Kalousová, K., Sotin, C., 2020. The insulating effect of methane clathrate crust on Titan's thermal evolution. Geophys. Res. Lett. 47 (13), e2020GL087481. http://dx.doi.org/10.1029/2020GL087481.

Kang, W., Mittal, T., Bire, S., Campin, J.-M., Marshall, J., 2022. How does salinity shape ocean circulation and ice geometry on Enceladus and other icy satellites? Sci. Adv. 8 (29), eabm4665. http://dx.doi.org/10.1126/sciadv.abm4665.

Kärnä, T., Legat, V., Deleersnijder, E., 2013. A baroclinic discontinuous Galerkin finite element model for coastal flows. Ocean Model. 61, 1–20. http://dx.doi.org/10.1016/j.ocemod.2012.09.009.

Kell, G.S., 1975. Density, thermal expansivity, and compressibility of liquid water from 0. deg. to 150. deg.. Correlations and tables for atmospheric pressure and saturation reviewed and expressed on 1968 temperature scale. J. Chem. Eng. Data 20 (1), 97–105. http://dx.doi.org/10.1021/je60064a005.

Kvorka, J., Čadek, O., Tobie, G., Choblet, G., 2018. Does Titan's long-wavelength topography contain information about subsurface ocean dynamics? Icarus 310, 149–164. http://dx.doi.org/10.1016/j.icarus.2017.12.010.

Lefevre, A., Tobie, G., Choblet, G., Čadek, O., 2014. Structure and dynamics of Titan's outer icy shell constrained from Cassini data. Icarus 237, 16–28. http://dx.doi.org/10.1016/j.icarus.2014.04.006.

Lunine, J.I., Stevenson, D.J., 1987. Clathrate and ammonia hydrates at high pressure: Application to the origin of methane on Titan. Icarus 70 (1), 61–77. http://dx.doi.org/10.1016/0019-1035(87)90075-3.

Marotzke, J., 1991. Influence of convective adjustment on the stability of the thermohaline circulation. J. Phys. Oceanogr. 21 (6), 903–907. http://dx.doi.org/10.1175/1520-0485(1991)021<0903:IOCAOT>2.0.CO;2.

Matsuyama, I., 2014. Tidal dissipation in the oceans of icy satellites. Icarus 242, 11–18. http://dx.doi.org/10.1016/j.icarus.2014.07.005.

Matsuyama, I., Beuthe, M., Hay, H.C., Nimmo, F., Kamata, S., 2018. Ocean tidal heating in icy satellites with solid shells. Icarus 312, 208–230. http://dx.doi.org/10.1016/j.icarus.2018.04.013.

Mitri, G., Meriggiola, R., Hayes, A., Lefevre, A., Tobie, G., Genova, A., Lunine, J.I., Zebker, H., 2014. Shape, topography, gravity anomalies and tidal deformation of Titan. Icarus 236, 169–177. http://dx.doi.org/10.1016/j.icarus.2014.03.018.

Nimmo, F., Bills, B.G., 2010. Shell thickness variations and the long-wavelength topography of Titan. Icarus 208 (2), 896–904. http://dx.doi.org/10.1016/j.icarus.2010.02.020.

Okubo, A., 1971. Oceanic diffusion diagrams. Deep-Sea Res. 18, 789–802. http://dx.doi.org/10.1016/0011-7471(71)90046-5.

O'Rourke, J.G., Stevenson, D.J., 2014. Stability of ice/rock mixtures with application to a partially differentiated Titan. Icarus 227, 67–77. http://dx.doi.org/10.1016/j.icarus.2013.09.010.

Pacanowski, R., Philander, S., 1981. Parameterization of vertical mixing in numerical models of tropical oceans. J. Phys. Oceanogr. 11, 1443–1451. http://dx.doi.org/10.1175/1520-0485(1981)011<1443:POVMIN>2.0.CO;2.

Rappaport, N.J., Iess, L., Wahr, J., Lunine, J.I., Armstrong, J.W., Asmar, S.W., Tortora, P., Di Benedetto, M., Racioppa, P., 2008. Can Cassini detect a subsurface ocean in Titan from gravity measurements? Icarus 194 (2), 711–720. http://dx.doi.org/10.1016/j.icarus.2007.11.024.

Sears, W.D., 1995. Tidal dissipation in oceans on Titan. Icarus 113 (1), 39–56. http://dx.doi.org/10.1006/icar.1995.1004.

Smagorinsky, J., 1963. General circulation experiments with the primitive equations: I. the basic experiment. Mon. Weather Rev. 91 (3), 99–164. http://dx.doi.org/10.1175/1520-0493(1963)091<0099:GCEWTP>2.3.CO;2.

Soderlund, K.M., 2019. Ocean dynamics of outer solar system satellites. Geophy. Res. Lett. 46 (15), 8700–8710. http://dx.doi.org/10.1029/2018GL081880.

Soderlund, K., Schmidt, B., Wicht, J., Blankenship, D., 2014. Ocean-driven heating of Europa's icy shell at low latitudes. Nat. Geosci. 7 (1), 16. http://dx.doi.org/10.1038/ngeo2021.

Sohl, F., Hussmann, H., Schwentker, B., Spohn, T., Lorenz, R.D., 2003. Interior structure models and tidal Love numbers of Titan. J. Geophys. Res.-Planet. 108 (E12), http://dx.doi.org/10.10029/2003JE002044.

Sohl, F., Sears, W.D., Lorenz, R.D., 1995. Tidal dissipation on Titan. Icarus 115 (2), 278–294. http://dx.doi.org/10.1006/icar.1995.1097.

Sohl, F., Solomonidou, A., Wagner, F.W., Coustenis, A., Hussmann, H., Schulze-Makuch, D., 2014. Structural and tidal models of Titan and inferences on cryovolcanism. J. Geophys. Res.-Planet. 119 (5), 1013–1036. http://dx.doi.org/10.1002/2013JE004512.

Squire, V.A., 2007. Of ocean waves and sea-ice revisited. Cold Reg. Sci. Technol. 49 (2), 110–133. http://dx.doi.org/10.1016/j.coldregions.2007.04.007.

Squire, V.A., Dugan, J.P., Wadhams, P., Rottier, P.J., Liu, A.K., 1995. Of ocean waves and sea ice. Annu. Rev. Fluid Mech. 27 (1), 115–168. http://dx.doi.org/10.1146/annurev.fl.27.010195.000555.

Tobie, G., Gautier, D., Hersant, F., 2012. Titan's bulk composition constrained by Cassini-Huygens: implication for internal outgassing. Astrophys. J. 752 (2), 125. http://dx.doi.org/10.1088/0004-637X/752/2/12.

Tyler, R.H., 2008. Strong ocean tidal flow and heating on moons of the outer planets. Nature 456 (7223), 770–772. http://dx.doi.org/10.1038/nature07571.

Tyler, R.H., 2009. Ocean tides heat Enceladus. Geophys. Res. Lett. 36 (15), http://dx.doi.org/10.1029/2009GL038300.

Tyler, R.H., 2011. Tidal dynamical considerations constrain the state of an ocean on Enceladus. Icarus 211 (1), 770–779. http://dx.doi.org/10.1016/j.icarus.2010.10.007.

Tyler, R.H., 2014. Comparative estimates of the heat generated by ocean tides on icy satellites in the outer solar system. Icarus 243, 358–385. http://dx.doi.org/10.1016/j.icarus.2014.08.037.

Tyler, R.H., 2019. Tidal response of planetary fluids (TROPF): Tutorial and user's manual, with examples. http://dx.doi.org/10.5281/zenodo.3523274, URL: https://github.com/RobertHTyler/TROPF.

Tyler, R.H., 2020. Heating of Enceladus due to the dissipation of ocean tides. Icarus 348, 113821. http://dx.doi.org/10.1016/j.icarus.2020.113821.

Vance, S., Goodman, J., 2009. Oceanography of an ice-covered moon. Europa 459–484.

Vaughan, G.L., Bennetts, L.G., Squire, V.A., 2009. The decay of flexural-gravity waves in long sea ice transects. Proc. R. Soc. A: Math. Phys. Eng. Sci. 465 (2109), 2785–2812. http://dx.doi.org/10.1098/rspa.2009.0187.

Vincent, D., Karatekin, O., Lambrechts, J., Lorenz, R.D., Dehant, V., Deleersnijder, E., 2018. A numerical study of tides in Titan's northern seas, Kraken and Ligeia Maria. Icarus 310, 105–126. http://dx.doi.org/10.1016/j.icarus.2017.12.018.

Vincent, D., Karatekin, O., Vallaeys, V., Hayes, A.G., Mastrogiuseppe, M., Notarnicola, C., Dehant, V., Deleersnijder, E., 2016. Numerical study of tides in Ontario Lacus, a hydrocarbon lake on the surface of the Saturnian moon Titan. Ocean Dyn. 66 (4), 461–482. http://dx.doi.org/10.1007/s10236-016-0926-2.

Wadhams, P., Squire, V.A., Goodman, D.J., Cowan, A.M., Moore, S.C., 1988. The attenuation rates of ocean waves in the marginal ice zone. J. Geophys. Res.-Oceans 93 (C6), 6799–6818. http://dx.doi.org/10.1029/JC093iC06p06799.

Zeng, Y., Jansen, M.F., 2021. Ocean circulation on Enceladus with a High-versus Low-salinity ocean. Planet. Sci. J. 2 (4), 151. http://dx.doi.org/10.3847/psj/ac1114.

Zhu, P., Manucharyan, G.E., Thompson, A.F., Goodman, J.C., Vance, S.D., 2017. The influence of meridional ice transport on Europa's ocean stratification and heat content. Geophy. Res. Lett. 44 (12), 5969–5977. http://dx.doi.org/10.1002/2017GL072996.